

The ionosphere: effects, GPS modeling and the benefits for space geodetic techniques

Manuel Hernández-Pajares · J. Miguel Juan · Jaume Sanz ·
Àngela Aragón-Àngel · Alberto García-Rigo ·
Dagoberto Salazar · Miquel Escudero

Received: 1 July 2010 / Accepted: 13 August 2011
© Springer-Verlag 2011

Abstract The main goal of this paper is to provide a summary of our current knowledge of the ionosphere as it relates to space geodetic techniques, especially the most informative technology, global navigation satellite systems (GNSS), specifically the fully deployed and operational global positioning system (GPS). As such, the main relevant modeling points are discussed, and the corresponding results of ionospheric monitoring are related, which were mostly computed using GPS data and based on the direct experience of the authors. We address various phenomena such as horizontal and vertical ionospheric morphology in quiet conditions, traveling ionospheric disturbances, solar flares, ionospheric storms and scintillation. Finally, we also tackle the question of how improved knowledge of ionospheric conditions, especially in terms of an accurate understanding of the distribution of free electrons, can improve space geodetic techniques at different levels, such as higher-order ionospheric effects,

precise GNSS navigation, single-antenna GNSS orientation and real-time GNSS meteorology.

Keywords Ionospheric effects · Ionospheric modeling · Space Geodesy · GNSS · GPS

1 Introduction

Prior to the era of global navigation satellite systems (GNSS), ionospheric sounding was much more limited than it is today in terms of spatial and temporal sampling. For instance, the number of ionosondes was limited, and these provided only direct observations of the local bottomside electron density profile. These observations are obtained through a series of measurements of the travel times of two-way electromagnetic (EM) signals for an increasing series of frequencies. Even fewer incoherent scatter radar facilities were available due to their high cost, despite their capability for direct observation of the free-electron density distribution with tomographic resolution. In the GNSS era, however, the dual-frequency global positioning system (GPS) has become a type of global scanner of the Earth's ionosphere, or an *ionoscope*.

To provide an overview of ionospheric science as it relates to space geodetic techniques, we have organized this paper into five main sections:

- basic ionospheric morphology,
- basic models for GNSS in ionospheric sounding,
- electron content monitoring from GNSS data,
- short-term ionospheric variability based on GNSS observations,
- benefits of ionospheric knowledge for space geodesy.

M. Hernández-Pajares (✉) · J. M. Juan · J. Sanz · À. Aragón-Àngel ·
A. García-Rigo · D. Salazar · M. Escudero
Research Group of Astronomy and Geomatics (gAGE),
Technical University of Catalonia (UPC), Catalonia, Spain
e-mail: manuel@ma4.upc.edu

J. M. Juan
e-mail: miguel@fa.upc.edu

J. Sanz
e-mail: jaume@ma4.upc.edu

À. Aragón-Àngel
e-mail: angela@ma4.upc.edu

A. García-Rigo
e-mail: agarcia@ma4.upc.edu

D. Salazar
e-mail: Dagoberto.Jose.Salazar@upc.edu

M. Escudero
e-mail: escudero@ma4.upc.edu

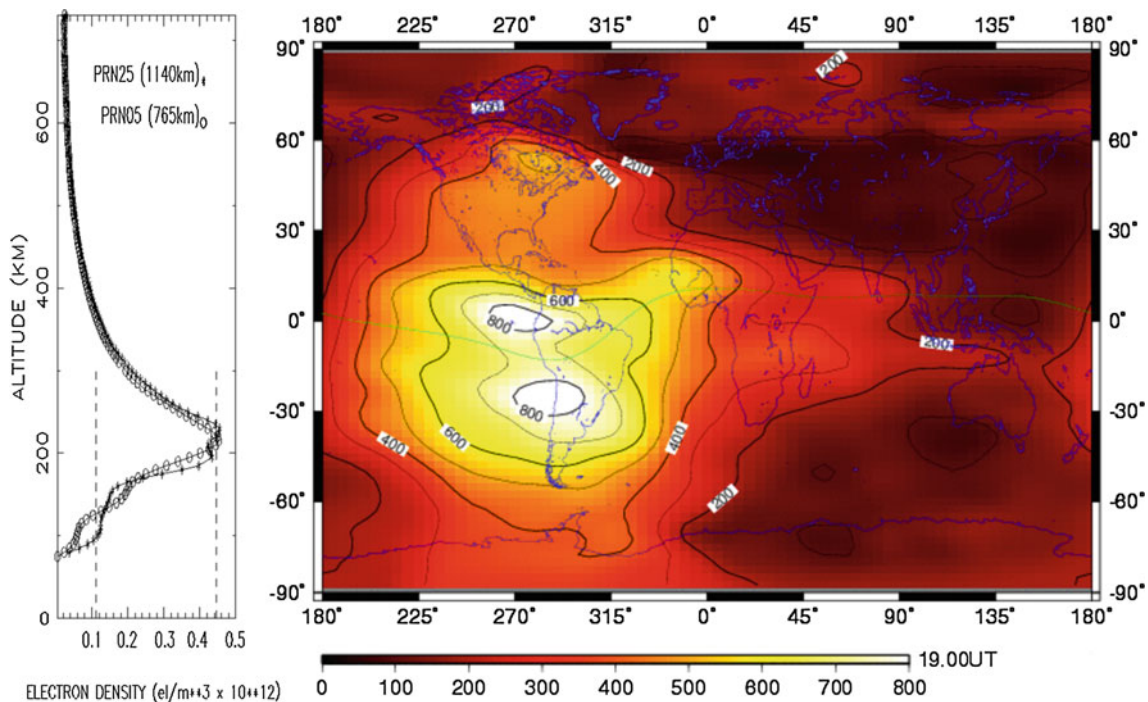


Fig. 1 Example of an electron density profile computed from radio occultation GPS for meteorology low earth orbiter (GPS/MET LEO) data (left) and example of VTEC map computed from ground based GPS data (right). The electron density is expressed in e/m^3 , as a function

of height, and the VTEC is expressed in tenths of $TECU = 10^{16} e^-/m^2$ (the major vertical gradients are found close to the Earth's geomagnetic equator, represented by the green line)

2 Basic ionospheric morphology

The ionosphere can be considered as the part of the Earth's atmospheric region that has enough ionized molecules and free electrons to significantly affect radio wave propagation. The main physical quantity adopted to characterize the ionosphere is the spatial and temporal distribution of the number of free electrons per volume unit (electron density N_e). This is due to its prevalent effect on radio wave propagation associated with its charge–mass ratio, which is much higher than those of ions. It typically extends from approximately 70 to 1,000 km above sea level, with its maximum effects found at heights of a few hundred kilometers, which is the altitude coinciding with the highest ionization (i.e., where the combination of abundant extreme ultraviolet (EUV) and X-ray solar radiation intensity and sufficient neutral atmospheric density cause an ionization maximum; for example, see the left panel in Fig. 1). The presence of ions and free electrons decreases above 1,000 km, although traces of free electrons are present up to altitudes of a few tens of thousands of kilometers in the plasmasphere or protonosphere (named after the H^+ ions predominant in this region; see Davies 1990 for more details).

2.1 Vertical distribution and electron density profiles

The vertical distribution of free electrons presents a density maximum at heights typically ranging from 200 to 400 km

(see the left panel of Fig. 1). As it has been indicated above, this distribution results from a compromise between sufficient EUV and X-ray ionizing radiation intensities (found mainly at high altitudes with low atmospheric absorption) and a sufficient density of molecules capable of being ionized (found mainly at low heights due to atmospheric hydrostatic equilibrium and the associated density increase with decreasing height). The electron density N_e can be described in terms of a simple first-principle approach, called Chapman model. Indeed, in hydrostatic equilibrium (the pressure scale height below that of the temperature scale), assuming an ideal gas, for a monochromatic beam acting on the lower part of the atmosphere, and considering the photochemical equilibrium, it can be demonstrated that (Davies 1990):

$$N_e(h, \chi) = N_{e,0} e^{\frac{1}{2} \left(1 - \frac{h-h_{m,0}}{H} - \sec \chi \right) e^{-\frac{h-h_{m,0}}{H}}} \quad (1)$$

where $N_{e,0}$ and $h_{m,0}$ represent the global electron density peak and corresponding height, respectively, and H the scale height (see Fig. 2 for a typical distribution of Chapman profiles, for various solar-zenith angles, χ , and heights, h).

2.2 Horizontal electron distribution, global VTEC maps and their temporal spectra

One useful physical quantity for describing the horizontal distribution of the electron content of the ionosphere is the

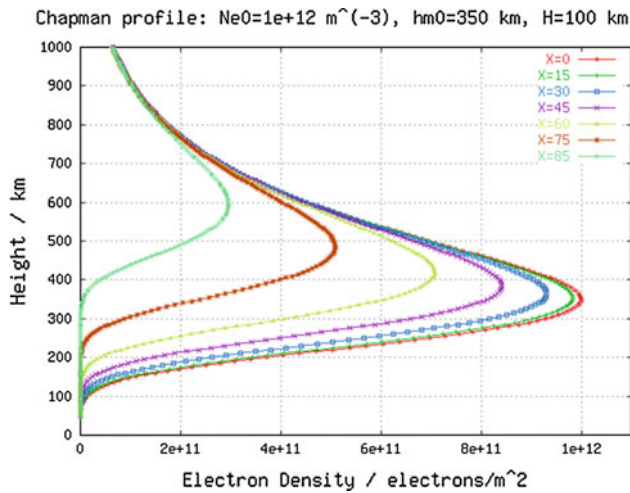


Fig. 2 Chapman electron density profiles corresponding to various solar-zenith angles χ (for 0, 15, 30, 45, 60, 75 and 85°)

vertical total electron content (VTEC). It is defined as the electron density integrated vertically; see Eq. 2,

$$V = \int_{r_0}^{r_1} N_e dr \tag{2}$$

where V represents VTEC, r the geocentric distance, and r_0 and r_1 are the minimum and maximum radial distance boundaries for the distribution of free electrons (realistic values are $r_0 \simeq 50$ km and $r_1 \simeq r_{GPS} \simeq 20,200$ km).

Looking at the global distribution of VTEC, maxima are observed on both sides of the geomagnetic equator (i.e., the equatorial or Appleton–Hartree anomaly) that are correlated with the Sun’s position (see the right panel in Fig. 1). This distribution is a manifestation of the phenomenon called the *equatorial fountain*. In brief, the electrons fall at both sides of the geomagnetic equator after experiencing the $\mathbf{E} \times \mathbf{B}$ drift generated by the horizontally northward magnetic field (\mathbf{B}) and, typically, an eastward electric field (\mathbf{E}) in the equatorial regions (Davies 1990). The remarkable result of this phenomenon is a bimodal distribution of electron density in terms of geomagnetic latitude, with maxima at approximately 15° from the geomagnetic equator.

The evolution of the electron content over time is dominated by several periods; the main one of approximately 11 years is associated with the solar cycle, in accordance with the solar flux. Figure 3 shows the evolution of the total number of free electrons, referred to as the global electron content (GEC), which is computed from global VTEC maps provided by the International GNSS Service (IGS). Other significant periods are the semi-annual or seasonal cycle (with maxima in spring and autumn, and minima in summer and winter) and the solar rotation period, lasting approximately 27 days;

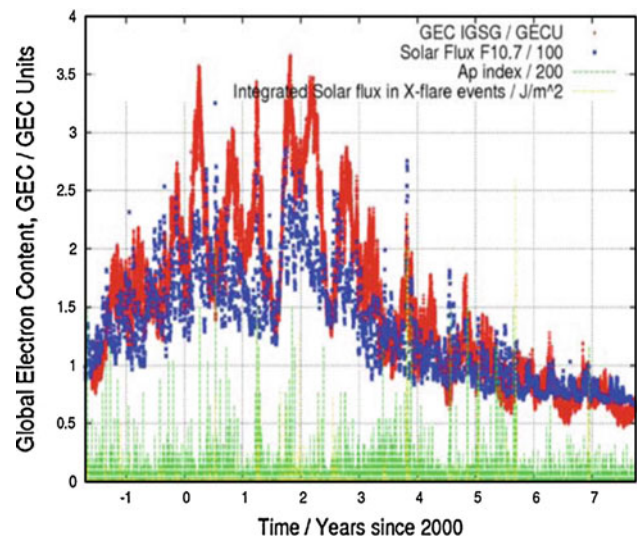


Fig. 3 Global electron content evolution (in GECU = 10^{32} electrons) during the availability of IGS ionospheric products versus solar flux, Ap index and X-ray flux, since 1 June, 1998 (source: Final IGS VTEC maps)

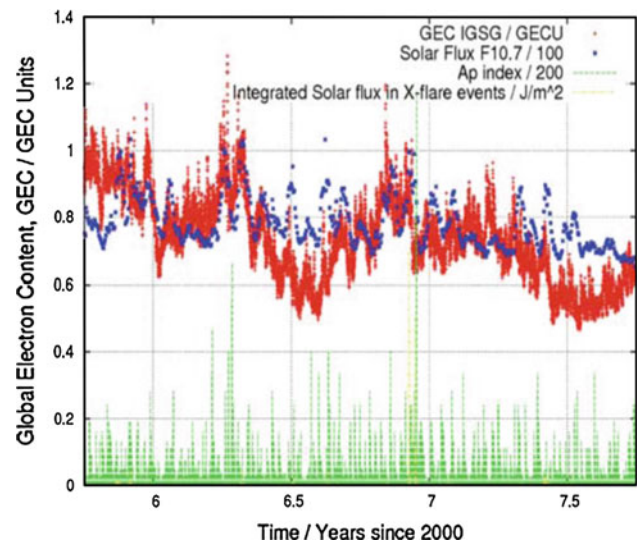


Fig. 4 Global electron content evolution during the availability of IGS ionospheric products versus solar flux, Ap index and X-ray flux, enlarged view from the end of 2005 to the beginning of 2008 (source: Final IGS VTEC maps)

see Fig. 4 for a more detailed plot and Hernández-Pajares et al. (2009a) for further details.

3 Basic models for GNSS in ionospheric sounding

The main direct ionospheric information provided by GNSS is the electron content, which can be derived from dual-frequency data. There are typically two basic measurements that are combined for this purpose: dual-frequency code pseud-

orange and carrier phase data. In both cases, the electron content is determined at the same time as the other associated unknowns are estimated, such as the phase ambiguities or interfrequency differential code biases.

3.1 Basic models for GNSS observables

Excellent monographs exist that introduce the fundamentals of GNSS (Hofmann-Wellenhof et al. 2008; Misra and Enge 2004 among others). The main terms related to ionospheric delay are briefly introduced here along with the notation used throughout the paper (more details on GNSS data processing can also be found in Sanz et al. 2011).

Both GNSS code and carrier phase measurements are defined as follows:

1. Code or pseudorange: This measurement is given by the apparent travel time τ of the EM signal propagated from GPS transmitter to receiver, scaled by the speed of light in the vacuum, c . This value can be partially considered as a range, i.e., a pseudorange $\tilde{\rho}$:

$$P \equiv c\tau = \tilde{\rho} \quad (3)$$

It is typically obtained by correlating the received pseudorandom noise code (PRN; a binary function similar to random noise and with very good correlation properties) with a replica implemented in the receiver. In GPS, the characteristic length (“chip” length) is approximately 300 m for the coarse acquisition code ($C \equiv C/A$) and 30 m for the precise code (P), which translate into typical measurement errors of approximately 1% (i.e., at the meter and decimeter levels for the C and P codes, respectively). Depending on the receiver environment and antenna/correlator characteristics, this error can be significantly increased (up to several meters or more) due to the multipath effects, showing a colored spectrum.

2. Carrier phase: This measurement is computed in the receiver by continuously integrating the frequency Doppler shift, primarily due to the relative velocity, clocks, and tropospheric and ionospheric drifts. This value is scaled in unit lengths in such a way that it represents the pseudorange $\tilde{\rho}$ and basically refers to the last time the carrier phase was locked by the receiver t_L (i.e., the pseudorange change since the last “cycle-slip” or the first acquisition epoch).

If we consider a planar wave moving in a certain direction, with a relative velocity c between the transmitter and the receiver, we can demonstrate that the received frequency change δf , with respect to the nominal one f ,

is given by:

$$\frac{\delta f}{f} = -\frac{\dot{\tilde{\rho}}}{c}, \quad (4)$$

where the dot represents the derivative with respect to time, c can be taken in our problem as the speed of light in vacuum, and $\dot{\tilde{\rho}}$ represents the pseudorange rate, including the geometric Doppler effect and the other effects mentioned above. By integrating the Doppler residual frequency at the receiver, it is possible to compute the variation of the pseudorange since the lock time t_L , as it refers to the current time t :

$$\int_{t_L}^t \dot{\tilde{\rho}} dt = -\frac{c}{f} \int_{t_L}^t \delta f \cdot dt. \quad (5)$$

Thus, the carrier phase is finally defined as:

$$L \equiv -\lambda \int_{t_L}^t \delta f \cdot dt = \tilde{\rho}(t) - \tilde{\rho}(t_L) = \tilde{\rho} + B_f, \quad (6)$$

where B_f is the carrier phase ambiguity for frequency f and $\lambda = c/f$ is the corresponding carrier wavelength. The characteristic wavelengths in GPS are those associated with the corresponding carriers: $f_1 = 154f_0$ for L_1 and $f_2 = 120f_0$ for L_2 , derived from the fundamental frequency $f_0 = 10.23$ MHz, i.e., $\lambda_1 \simeq 0.19$ m and $\lambda_2 \simeq 0.24$ m. For phase measurements, the error is approximately at millimeter level ($\simeq 0.01\lambda$), between two to three orders of magnitude smaller than the code measurement error. This fact, along with a much smaller multipath (less than $\frac{\lambda}{4} \simeq 0.05$ m, typically at the level of few millimeters) due to the beat phase characteristics, makes this observable the most suitable for high-accuracy applications in general and for ionospheric sounding in particular. Indeed, precise navigation and ionospheric determinations are usually made with carrier phase measurements. However, to best utilize the carrier phase, the large associated unknown (carrier phase ambiguity) must be properly solved, typically as an unknown parameter (treated as a Gaussian random variable) in a given continuous arc of data (with no cycle-slips, i.e., with no loss of lock on the signal).

3.1.1 Ionospheric delay/advance in GNSS code/phase measurements

By neglecting the frictional force and assuming a cold, collisionless, magnetized plasma, the ionospheric refractive index for the carrier phase can be expressed by the Appleton

formula (e.g., Davies 1990, page 72). Consequently, the ionospheric delay in the carrier phase $\delta\rho_{I,p}$ (which is negative, i.e., an advance) can be derived as Eq. 7 (for further details, see the corresponding section in the most recent update of the International Earth Rotation and Reference System Service, IERS, conventions, Hernández-Pajares et al. 2010b):

$$\delta\rho_{I,p} = -\frac{s_1}{f^2} - \frac{s_2}{f^3} - \frac{s_3}{f^4}, \tag{7}$$

with the following corresponding terms:

$$s_1 = 40.309 \int_{\mathbf{r}_T}^{\mathbf{r}_R} N_e dl, \tag{8}$$

$$s_2 = 1.1284 \cdot 10^{12} \int_{\mathbf{r}_T}^{\mathbf{r}_R} N_e B \cos \theta dl, \tag{9}$$

$$s_3 = 812.42 \cdot 10^{12} \int_{\mathbf{r}_T}^{\mathbf{r}_R} N_e^2 dl, \tag{10}$$

where B represents the magnetic field modulus at a given point on the transmitter-to-receiver line-of-sight (LOS) ray, θ is the angle between the magnetic field vector and the EM propagation vector, and \mathbf{r}_T and \mathbf{r}_R correspond to the geocentric position vector of the GNSS transmitter and receiver, respectively, N_e represents the density of free electrons (the number per volume unit), and dl is the length element. All constants are expressed in the International System of Units (SI), and the term s_3 has been approximated by the dominant term.

Moreover, the code ionospheric delay $\delta\rho_{I,c}$ has also been shown to fulfill the following relationship with the carrier phase ionospheric delay $\delta\rho_{I,p}$ (e.g., Seeber 1993):

$$\delta\rho_{I,c} = \delta\rho_{I,p} + f \frac{d}{df} \delta\rho_{I,p}. \tag{11}$$

From the previous Equation, and Eq. 7, the corresponding expression for the code ionospheric delay up to the third order can be derived as follows:

$$\delta\rho_{I,c} = \frac{s_1}{f^2} + 2\frac{s_2}{f^3} + 3\frac{s_3}{f^4}. \tag{12}$$

The first-order term (with a dependence on f^{-2}) has been shown to account for more than 99.9% of the total ionospheric delay in both the GNSS code (the delay) and the carrier phase (the advance; see, for instance, Hernández-Pajares et al. 2010b). As a result, the first-order term becomes an excellent approximation to work with (Eqs. 7 and 8):

$$\delta\rho_{I,p} = -\delta\rho_{I,c} = -\frac{40.309}{f^2} S, \tag{13}$$

where

$$S = \int_{\mathbf{r}_T}^{\mathbf{r}_R} N_e dl \tag{14}$$

is the slant total electron content (STEC). Owing to main dependency expressed in Eq. 13, it is possible to isolate the STEC, S , when simultaneous measurements are available at different frequencies (preferably carrier phases) from the same GNSS satellite and from a given receiver (see below Eqs. 17 and 29).

Additionally, Hernández-Pajares et al. 2010b also showed that at GNSS frequencies, most of the remaining higher-order ionospheric effects can be well approximated using just the second-order term (see Eqs. 7 and 9). Moreover, in that review, the relevance of the geometric bending at low elevation was also discussed for the GNSS ground-based data, based on the findings of Jakowski et al. (1994) and Hoque and Jakowski (2008). Practical aspects of interest in precise geodetic GPS positioning applications may be found in Hernández-Pajares et al. 2007 (e.g., the significant impacts on GPS satellite orbits and clocks, among others).

3.2 Basic model for GNSS combination of observables

Beyond the ionospheric delay discussed above, those additional terms affecting the apparent propagation time τ must be taken into account if they are significant at the level of the above-mentioned code and phase measurement errors (approximately at meter and millimeter level, respectively):

$$P_m = \rho + c(dt - dt') + \frac{40.309}{f_m^2} S + T + D_m + D'_m \tag{15}$$

and

$$L_m = \rho + c(dt - dt') - \frac{40.309}{f_m^2} S + T + B_m + \frac{c}{f_m} \phi \tag{16}$$

here, in SI units, P_m and L_m represent the code and phase measurements, respectively, of the transmitter by the receiver at a given time t , after correcting for the corresponding antenna phase center offset and vector; ρ , dt , dt' , S and T are the corresponding distance, receiver and transmitter clock errors, slant total electron content and slant tropospheric delay respectively; f_m refers to the frequency of the carrier “ m ”; D_m and D'_m are the receiver and transmitter inter-frequency differential code biases (DCBs), respectively, for the given frequency also referred to as interfrequency bias, IFB (note that the “prime” symbol represents terms associated with the GNSS transmitter/satellite). Finally, ϕ represents the relative rotation, in cycles, between the transmitter and receiver antennas (the wind-up effect associated with the

right-handed polarized GPS signal), and B_m represents the previously introduced carrier phase ambiguity.¹

In this context the STEC dependency can be isolated using dual frequency measurements. Indeed, in the case of the fully operational GPS system, both ionospheric combinations of carrier phases and pseudoranges can be defined as:

$$L_I \equiv L_1 - L_2 = \alpha \cdot S - \beta \cdot \phi + B_I, \quad (17)$$

$$P_I \equiv P_2 - P_1 = \alpha \cdot S + D_I + D'_I + \epsilon_M + \epsilon_T, \quad (18)$$

where $\alpha = 40.309 \left(\frac{1}{f_2^2} - \frac{1}{f_1^2} \right) = 1.05 \cdot 10^{-17} \text{ m}^3$, $\beta = c \left(\frac{1}{f_2} - \frac{1}{f_1} \right) = 0.054 \text{ m}$, $B_I = B_1 - B_2$, $D_I = D_2 - D_1$ and $D'_I = D'_2 - D'_1$.² In this case, we also made explicit the two main components of the measurement error, both corresponding to the code: the multipath code error ϵ_M and the thermal noise measurement error ϵ_T . Typically, the wind-up term $\beta \cdot \phi$ is a centimeter-level term. For the permanent receivers, this term can be corrected very accurately from their coordinates and orbital information, and it is not discussed explicitly herein.

The measurement errors for the P_I and C_I codes are approximately at submeter and several meters levels, respectively, neglecting multipath error sources and assuming Gaussian independent measurement error distributions for both frequencies. Similarly, the measurement error for L_I can be estimated at the millimeter level.

4 Electron content monitoring from GNSS data

To estimate the ionospheric electron content distribution from GNSS observables such as L_I and P_I (see Eqs. 17 and 18), several considerations must be taken into account.

First, in the very precise ionospheric observable L_I , the varying term is basically the STEC, S : indeed, the ambiguity B_I , which also contains the phase instrumental delays, can be considered constant for a continuous arc of data, and the observable is almost unaffected by noise (thermal noise at the millimeter level and with a multipath error typically much lower than 0.01 m), especially when compared with the code. In spite of the fact that similar reasoning can be applied to P_I (the interfrequency differential code biases are

typically considered constant at a daily scale), the thermal noise and especially the code multipath error can drive the apparent evolution of the P_I observables from time scales of seconds to minutes.

In general, the electron content is typically estimated in the ionospheric filter simultaneously with the carrier phase ambiguities or DCBs. If the main goal is to determine the STEC from ionospheric GNSS observables, we can consider three main procedures (listed in order from high to low complexity):

1. Estimating the phase ambiguities B_I simultaneously as parameters of a geometric model of the electron content (see below). This procedure implies that for N_R receivers and N_T GNSS transmitters, a typically large number of $N_R \cdot N_T$ unknown phase ambiguities must be estimated.
2. The number of unknowns associated with the estimation of B_I can be dramatically reduced with a precise geodetic model with static GNSS receivers. In this case, the receiver position is known at the centimeter level, and two linearly independent combinations of the ambiguities B_1 and B_2 can usually be determined based on a few minutes of data: the ionospheric-free combination ambiguity (B_c , Eq. 19 using the precise coordinates of the receiver and precise orbits and clocks provided for example by IGS, Dow et al. 2009), and the wide-lane carrier phase ambiguity (B_w , Eq. 20, by averaging the corresponding Melbourne-Wübbena combination, Hernández-Pajares et al. 2002). This approach is extendable to Galileo and GPS modernized signals and has excellent potential for real-time applications due to the third frequency and extra-widelane carrier-phase combinations (see for example Hernández-Pajares et al. 2003). The basic relationships defining B_c and B_w ambiguities are:

$$B_c = \frac{f_1^2 B_1 - f_2^2 B_2}{f_1^2 - f_2^2}, \quad (19)$$

$$B_w = \frac{f_1 B_1 - f_2 B_2}{f_1 - f_2} \quad (20)$$

associated with the corresponding ionospheric-free and widelane carrier phase combinations:

$$L_c = \frac{f_1^2 L_1 - f_2^2 L_2}{f_1^2 - f_2^2}, \quad (21)$$

$$L_w = \frac{f_1 L_1 - f_2 L_2}{f_1 - f_2}. \quad (22)$$

These relationships are processed together with their respective codes:

¹ In fact, the carrier phase ambiguity can be expressed as $B_m = \lambda_m \cdot N + \delta B_m + \delta B'_m$, i.e., an integer number of N cycles and phase instrumental delays, a fractional term depending on the receiver δB_m and a fractional term depending on the satellite $\delta B'_m$. Strictly speaking, only the integer number of cycles is constant; the fractional part cancels out when simultaneous double differences between pairs of transmitters and receivers are considered. As a consequence, they do not affect directly the carrier phase ambiguity fixing (Ge et al. 2008).

² For GPS, these variables satisfy the defining conditions $f_2^2 D_2 = f_1^2 D_1$ and $f_2^2 D'_2 = f_1^2 D'_1$ associated with a value of zero for the ionospheric-free combination of P_1 and P_2 delay-code biases, which define the origin of the clock corrections.

$$P_c = \frac{f_1^2 P_1 - f_2^2 P_2}{f_1^2 - f_2^2}, \tag{23}$$

$$P_n = \frac{f_1 P_1 + f_2 P_2}{f_1 + f_2}. \tag{24}$$

In this last case, the Melbourne-Wübbena combination $M_w = L_w - P_n$ can be formed. From here on, it is straightforward to deduce that the phase ambiguity B_I of the ionospheric combination of carrier phases $L_I = L_1 - L_2$ (see Eq. 17) can be computed from B_c and B_w (which helps in the determination of the electron content in ionospheric models based on permanent GNSS receiver data; see the corresponding subsection below):

$$B_I \equiv B_1 - B_2 = \frac{\lambda_1 \lambda_2}{\lambda_w \lambda_n} [B_w - B_c] \tag{25}$$

considering

$$B_w = M_w - \frac{\lambda_w \lambda_n}{\lambda_1 \lambda_2} (D_I + D'_I) \tag{26}$$

where $\lambda_w = c/(f_1 - f_2)$ and $\lambda_n = c/(f_1 + f_2)$ represent the wavelengths of the widelane and narrowlane combinations, respectively. In this way, B_I can be expressed in terms of M_w , B_c (both very well known from the geodetic processing at the decimeter and centimeter levels, respectively) and the unknown interfrequency differential code biases D_I and D'_I :

$$B_I = \frac{\lambda_1 \lambda_2}{\lambda_w \lambda_n} [M_w - B_c] - D_I - D'_I \tag{27}$$

Thus, only $N_T + N_R$ extra unknowns are needed (compared to $N_T \cdot N_R$ for the previous approach) when the interfrequency differential code biases are estimated at the same time as parameters of the geometric electron content model describing S from the ionospheric carrier phase, corrected³ by the terms given by the precise geodetic modeling:⁴

$$L_I^* \equiv L_I - \frac{\lambda_1 \lambda_2}{\lambda_w \lambda_n} [M_w - B_c] = \alpha \cdot S - D_I - D'_I \tag{28}$$

Once the ionospheric carrier phase has been corrected for the ionospheric ambiguity (L_I^*), the STEC can be obtained with a similar absolute accuracy as $D_I + D'_I$, by adding the DCBs to L_I^* , typically at the TECU level.

³ This correction term only adds an error of approximately 1 TECU = 10^{16} e⁻/m² to the carrier phase, especially in cases where the majority of double-differenced ambiguities can be fixed in geodetic processing, see, for example, Hernández-Pajares et al. (2002).

⁴ The wind-up term ϕ is implicitly assumed to be already corrected, as indicated above.

3. A simpler but typically less accurate way of directly obtaining the STEC from ionospheric GNSS observables is to compute the ionospheric phase ambiguity aligning L_I with P_I :

$$B_I = \langle L_I - P_I \rangle + D_I + D'_I, \tag{29}$$

where $\langle \rangle$ stands for the average value for a period with coherent carrier phase data, i.e., without cycle-slip disrupting the continuity of these types of precise measurements. During this time interval, which can reach up to several hours, the DCBs can be considered constant, if the instrumentation remains the same. Nevertheless, for this approach, the accuracy may be worse due to uncertainties in and/or mismodeling of the interfrequency code biases and the code multipath (e.g., Ciraolo et al. 2007; Juan et al. 1997). Moreover, the thermal noise of the P_I combination is significantly higher than that of the Melbourne-Wübbena combination.

To provide regional or global maps of electron content, we need a model taking into account the geometric dependency of the GNSS-derived STECs. This model can be generated by discretizing, in length elements δl_i , the integral path that defines the STEC S , which in turn depends on the time t and the receiver and transmitter positions \mathbf{r}_R and \mathbf{r}_T , respectively:

$$S \equiv S(\mathbf{r}_R, \mathbf{r}_T, t) = \int_{\mathbf{r}_T}^{\mathbf{r}_R} N_e(\mathbf{r}', t) d\mathbf{l} \simeq \sum_{i=1}^n (N_e)_i \delta l_i, \tag{30}$$

and considering at every subionospheric point (placed at a geocentric distance r') the de-projection factor for the given LOS ray zenith angle $\chi' = 90 - E'$ degrees (see Fig. 5):

$$S \simeq \sum_{i=1}^n \frac{(N_e)_i \delta r_i}{\frac{\delta r_i}{\delta l_i}} = \sum_{i=1}^n \frac{\delta V_i}{\cos \chi'_i} = \sum_{i=1}^n M_i \delta V_i \tag{31}$$

where δV_i is the partial vertical electron content of the i th layer or shell and

$$M_i = \frac{1}{\cos \chi'_i} = \frac{1}{\sqrt{1 - \left(\frac{r}{r'_i}\right)^2 \cos^2 E}} \tag{32}$$

is the mapping function at the subionospheric point in the i th layer (see Fig. 5 and its caption for further details).

The optimal relationship between slant and VTEC ($V \equiv \delta V_1$ with a single layer $n = 1$ comprising the complete ionosphere) corresponds to an effective ionospheric geocentric distance r'_{IPP} with mapping M_{IPP} associated with a certain ionospheric pierce point (IPP):

$$S = M_{\text{IPP}} V_{\text{IPP}} \tag{33}$$

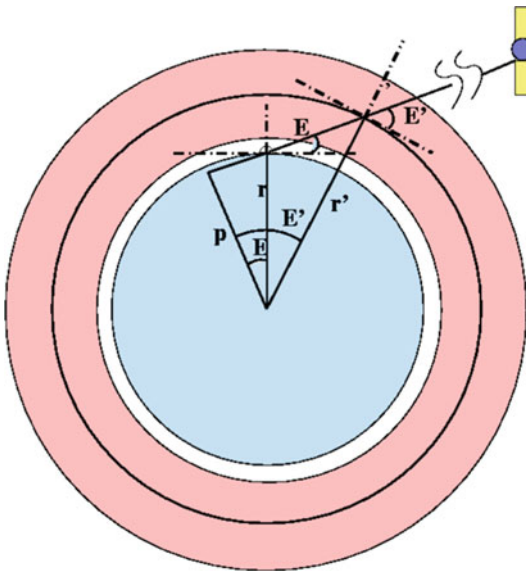


Fig. 5 The layout of the typical observation geometry, considering an ionospheric effective geocentric distance r' and a subionospheric elevation E' of the GNSS transmitter (r and E represent the geocentric distance and elevation observed from the permanent GNSS receiver, respectively, and p is the impact parameter)

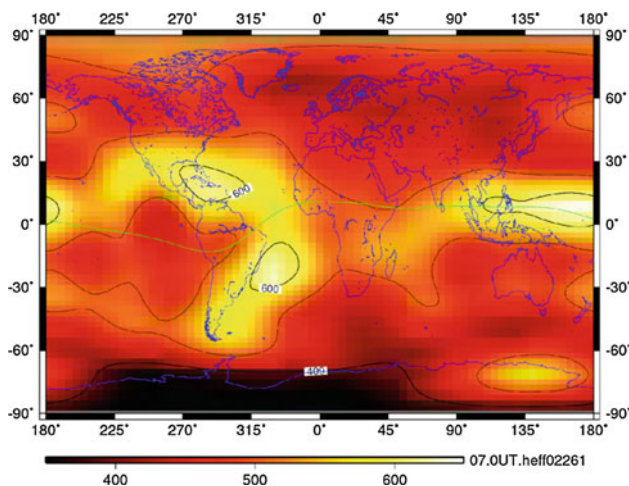


Fig. 6 Example of a GPS ionospheric effective height (in km) computed by the Technical University of Catalonia (UPC) from global IGS network data for 0700 Universal Time (UT), day 261 of 2002

This effective height (or equivalently the corresponding effective ionospheric height) and the associated mapping function can be chosen to minimize the error of this 2D approximation of the free-electron distribution (see Komjathy and Langley 1996). Note that the effective ionospheric height varies quite significantly on a global scale, as shown in Fig. 6, which was constructed from data from a previous study on a global ground based GPS solution (Hernández-Pajares et al. 2005a).

Nevertheless, many authors and ionospheric agencies still adopt a simpler approach: a fixed ionospheric height for the

whole ionosphere. This approach can induce errors ranging from a few TECU at middle latitudes up to 10 TECU or more in the equatorial regions (Smith et al. 2008; Hernández-Pajares et al. 1999).

At this point, it is important to emphasize that the computation of STEC from a given VTEC map should be performed with the same mapping function as previously used to compute the original VTEC map. Otherwise, the results can be degraded, jeopardizing any improvement associated with a better mapping function.

Finally, if we are interested in computing the electron density distribution from GNSS data, the main equation can be expressed as the above-introduced Eq. 30. The predominant vertical geometry of the ground-based GNSS data allows only poor vertical resolution, but this resolution is good enough to provide effective ionospheric heights. This detail is important in enabling the computation of very accurate real-time STECs, supporting, for instance, long-distance decimeter error-level GNSS navigation (see Hernández-Pajares et al. 2000b). However, to perform a detailed tomographic determination when much better vertical resolution is intended, additional data with complementary geometry are required such as low earth orbiter (LEO) GNSS dual-frequency occultation data (e.g., Jakowski et al. 2003; Hernández-Pajares et al. 2000a) or ionosonde data (García-Fernández et al. 2003a) or the use of a background model (e.g., the electron density assimilative model, EDAM; Angling and Cannon 2004).

4.1 Pseudorange interfrequency differential code biases and carrier phase ambiguities

The pseudorange interfrequency biases and carrier phase ambiguities deserve special attention due to their association with STEC in the corresponding ionospheric estimation, which may incorporate code measurements.

As discussed in the previous sections, the ionospheric combination of code pseudoranges can be used to level the ionospheric combination of carrier phases. Thus, the accuracy of the resulting STEC observable directly depends on the satellite and receiver DCB accuracies. Estimates of the actual precision for the satellite and receiver DCBs within the framework of the IGS are typically about 0.1 and 1 ns, respectively (Hernández-Pajares 2004). This precision basically transfers into an error in the carrier phase leveling (not considering multipath and other sources of biases) of about 3 TECUs (48 cm in L1). It is important to take into account that a typical error in the DCB determination is a bias. This happens for instance when the DCBs are computed simultaneously to the VTEC with a single layer electron content model (instead of using a multilayer description; see Juan et al. 1997) or from an isolated DCB receiver (instead of using a wide network), with higher DCB–VTEC correlations. Taking

into account the above-mentioned differences in the DCB and TEC strategies, biases in the DCBs of up to 7 ns in equatorial zones have been reported when comparing different single-station methods (Arikan et al. 2007). These results propagate into TEC differences of up to 21 TECU (more than 3 m in L1).

When using only carrier phase observables to derive STEC observables, the phase ambiguities (or DCBs when ambiguities derived from geometric modeling are used) must be determined simultaneously with the electron content (Eqs. 17 or 28, or the average electron density in Eq. 30). This can be done taking advantage of the change of geometry between epochs.

Another remarkable point concerns the impact of using 2D versus 3D ionospheric descriptions of the electron content, particularly when the carrier phase ambiguities or DCBs are computed simultaneously with the electron content. Although 2D models are simpler, they will always need a mapping function to derive the TEC observables. This point can be a significant limitation due to the inherent errors, which are especially important around the equatorial zone and during days of high geomagnetic activity. These 2D models, generally speaking, may be either regional, using polynomials to describe the ionosphere (Sardon et al. 1994; Ciraolo et al. 2007), or global using spherical harmonic expansions to represent the ionosphere (Schaer 1999; Brunini et al. 2003), or other evolved mathematical models such as B-splines (Schmidt et al. 2008) and multivariate adaptive regression splines (MARS, Durmaz et al. 2010). In 3D models, the complexity increases, requiring a more sophisticated but still affordable modeling of the ionosphere, e.g., empirical orthogonal functions (Howe et al. 1998), voxels (Hernández-Pajares et al. 1999; García-Fernández et al. 2003a,b) or vertical profile functions (Feltens 2007), among others.

Another important practical point concerns the reference system chosen to estimate the electron content model. Systems in which the free-electron distribution is more stationary (such as a solar fixed reference frame; see for example, Hernández-Pajares et al. 1999 using the geomagnetic latitude or Azpilicueta et al. 2006, using the modip latitude) present some advantages compared with others such as a terrestrial fixed reference system (see, for instance, Sardon et al. 1994). Indeed, due to the smaller associated temporal variability of electron density, a smoother filtering estimation (with much less process noise) can be applied when an ionospheric stationary reference system is used.

It is also worth mentioning that there is a new way of computing TEC by means of the global assimilation ionospheric models (GAIMs), which incorporates different data types as described in several publications (e.g., Angling and Cannon 2004; García-Fernández et al. 2003a,b; Hernández-Pajares et al. 1998). Moreover first principle physics can be used (e.g., JPL GAIM, see Hajj et al. 2004 or the IonoNumerics model, see Khattatov et al. 2006).

4.2 Examples of global models of electron content

An important application of the availability of GNSS data in global networks (such as those of the IGS, see Dow et al. 2009) is the computation of electron content distribution on a global scale for the whole ionosphere. An excellent review of ionospheric imaging can be found in Bust and Mitchell 2008. Representative works in global VTEC mapping include Mannucci et al. 1998; Schaer 1999, and Hernández-Pajares et al. 2009a.

Indeed, considering that the main GNSS measurement (the ionospheric carrier phase L_I) is proportional to STEC, i.e., proportional to the integrated electron density N_e along the ray path (see Eqs. 14, 17), an expression for N_e can be developed using certain basis functions. Two examples of such derivations use spherical harmonics (SH, 2D) and volume elements (voxels, 3D).

4.2.1 Example of a 2D estimation of global electron content: spherical harmonic basis functions

We express the electron contribution of a differential element of the path integral, Eq. 14, defining the STEC from its slant and radial length elements (dl and dr , respectively) through the slant factor (or mapping function M , typically Eq. 32):

$$N_e \cdot dl = \left(\frac{dl}{dr} \right) N_e \cdot dr = M \cdot N_e \cdot dr \quad (34)$$

Considering a 2D spherical electron density distribution, at a fixed effective ionospheric geocentric distance r_I , the following simple expression can be derived from Eqs. 14 and 34:

$$L_I = \alpha \cdot M \cdot V + B_I \quad (35)$$

where $V = \int_{r_T}^{r_R} N_e dr$ means the VTEC, and where the carrier phase ambiguity B_I term can be computed (for instance) from the corresponding code and DCBs (Eq. 29). Alternatively, and even better, the electron content model can be solved simultaneously with the phase ambiguities, or with the DCBs due to Eq. 28 in the context of a precise geodetic modeling.

Then, developing the VTEC in terms of the basis of SH $Y_{m,n}$ (which can be expressed as a function of the local time and colatitude), the following expression can be obtained for L_I :

$$L_I \simeq \alpha \cdot M \cdot \sum_m \sum_n a_{m,n} Y_{m,n} + B_I \quad (36)$$

In this approach, the main unknowns (apart from the ambiguities) to be estimated from the observations are the SH coefficients $a_{m,n}$, which, in general, should be treated as a random process (typically a random walk) in the context of batch least mean squares (LMS) or Kalman filter context, as

they typically evolve over time (Schaer 1999). The ambiguities can be estimated: (a) directly from Eq. 36 (due to the change of LOS geometry); (b) via, to a very good modeling of the geometric problem (Eq. 27); or (c) aligning the code with the phase plus the DCBs (Eq. 29), as described above. This approach and others, such as B-splines (Schmidt et al. 2008), are specially suitable when there is nearly homogeneous distribution of measurements at the global scale and when the resolution can be selected by adjusting more or fewer terms in the derivation. However, this SH computation may not be suitable when the distribution of data is not homogenous (as it occurs due to the lack of global GNSS data in the southern hemisphere and over the oceans), or if great local detail is needed (due to the global influence of SH functions).

4.2.2 Example of a 3D estimation of global electron content: voxel-based modeling

A different approach, one which overcomes the poor accuracy associated with the assumption of a fixed spherical height, as mentioned above, involves using a direct 3D derivation of the electron density N_e to estimate the global VTEC model. This example is based on volume elements, or voxel basis functions $P_{i,j,k}(\mathbf{r})$, defined as 1 if \mathbf{r} is closer to the voxel center $\mathbf{r}_{i,j,k}$ than to the other voxel centers and defined 0 otherwise. This model can be considered to be a special application of the so-called Voronoi decomposition (or tessellation) to the problem of ionospheric determination (see for example Du et al. 1999).

Discretizing N_e as a Voronoi decomposition gives:

$$N_e = \sum_i \sum_j \sum_k (N_e)_{i,j,k} \cdot P_{i,j,k}. \quad (37)$$

Considering that by the above definition of P , the length segment of the transmitter–receiver ray intersection with voxel $i - j - k$ ($\Delta l_{i,j,k}$) can be expressed as:

$$\Delta l_{i,j,k} = \int_{\mathbf{r}_T}^{\mathbf{r}_R} P_{i,j,k} dl, \quad (38)$$

and the main observation, Eq. 17, based on the ionospheric carrier phase, can be written (using Eq. 30) as:

$$L_I \simeq \alpha \cdot \sum_i \sum_j \sum_k (N_e)_{i,j,k} \cdot \Delta l_{i,j,k} + B_I \quad (39)$$

This approach (Juan et al. 1997; Hernández-Pajares et al. 1997b, 1999) is suitable, not only for avoiding the VTEC mismodeling associated with a fixed height 2D assumption of the electron content distribution, but also for obtaining local details, due to the limited scope of every basis function $P_{i,j,k}$. However the optimal number of layers depends on the specific scenario. If LEO-based GNSS data are available, the average electron density for many layers can be solved (Hernández-Pajares et al. 1998) or, even more efficiently, we can use the Abel transform inversion (Hernández-Pajares

et al. 2000a), as shown below. If only ground-based GNSS data are available, two layers are sufficient (Hernández-Pajares et al. 1999).

4.2.3 Interpolation and global VTEC maps

An important point in electron content estimation at global scale is the interpolation strategy adopted to provide reasonable values over large regions without the availability of ground GNSS measurements (this applies mainly to the southern hemisphere and the oceans). Despite the use of a background model (such as the International Reference Ionosphere, IRI, Bilitza 2001), the ionospheric variability in such large gaps of data (some of them ranging over few thousand kilometers) typically leads to better results when interpolation strategies based on actual data are used. In this regard, one example of an optimal interpolation algorithm for GNSS data is the Kriging technique, which is based on the assumption of an error decorrelation function with distance and direction, and is able to provide improvements of up to 10% or more relative to other techniques (see Orús et al. 2005).

4.2.4 Combination of global VTEC maps

Another way of improving the results, in terms of accuracy, integrity and the availability of global VTEC maps, is to combine VTEC maps computed with independent algorithms from different analysis centers. This strategy is applied for the final and the rapid IGS VTEC maps computed with latencies of 11 and 2 days respectively, resulting from an optimal combination of VTEC from four analysis centers (CODE, ESA, JPL and UPC) and involving, in particular, VTEC maps computed by means of spherical harmonics (CODE) and those computed with the Voronoi tessellation model (UPC). The resulting maps, with resolution of 2 h, 5° and 2.5° in UT, longitude and latitude, respectively, present a typical accuracy ranging from a few TECU to approximately 10 TECU in VTEC, depending on the solar cycle phase, latitude, local time and geomagnetic activity (see Hernández-Pajares et al. 2009a).

4.3 Example of a technique for direct electron density retrieval with radio occultation data

The first radio occultation experiments were designed and implemented in the Solar System probes during the late 1960s and 1970s (Kliore et al. 1967). Hajj et al. (1994) was probably one of the first authors to point out the strong potential of GPS data to perform 3D ionospheric tomography, due to direct limb observations of the STEC, which is directly dependent on the vertical distribution of the density of free electrons. Since the very first GPS radio occultation mission on the limb of the Earth, the GPS-MET (1994–1997, Ware et al. 1995),

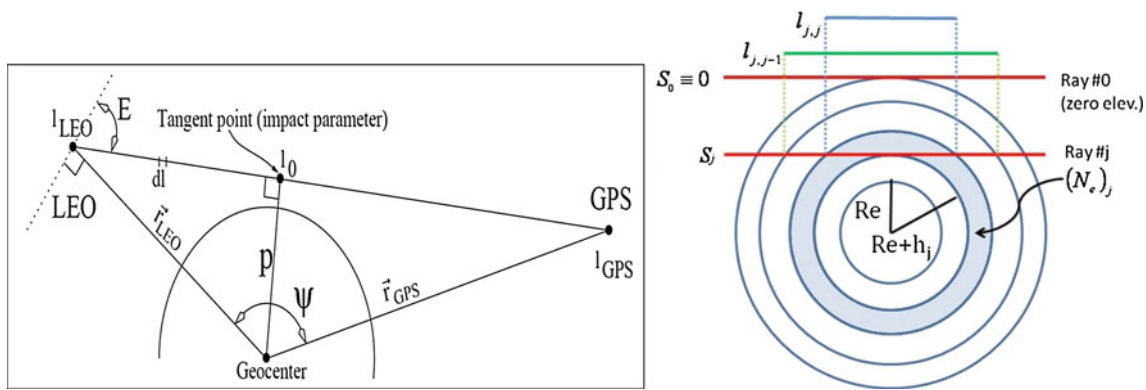


Fig. 7 *Left panel:* layout for occulting ray with impact parameter p during an occultation event, assuming a straight ray path. *Right panel:* spherical symmetry layout for occulting rays during an occultation

several occultation missions have been successfully developed and scientifically exploited (such as the “CHALLENGING Mini-Satellite Payload”, CHAMP, the “Satellite de Aplicaciones Cientificas - C”, SAC-C, and the “Gravity Recovery and Climate Experiment”, GRACE) in an effort to derive characteristic parameters of the Earth’s atmosphere. More recently, a full constellation of six LEO satellites (“Constellation Observing System for Meteorology, Ionosphere, and Climate”, COSMIC, also known as the FORMOSAT-3 mission) was deployed with onboard radio-occultation GPS receivers. The COSMIC / FORMOSAT-3 mission can provide up to $\approx 2,500$ daily occultations, whereas GPS/MET provided only ≈ 250 , CHAMP and SAC-C provided ≈ 400 .

The importance of LEO GNSS data goes beyond the capability of directly retrieving the full electron density profile below the LEO limit, as discussed in the next subsections. Indeed, the even global distribution of occultation events is a key to improving the global VTEC maps, which suffer from the lack of ground GNSS data in the southern hemisphere and over the oceans. This problem could be significantly mitigated by properly taking into account the VTEC values associated with the derived profiles (Alizadeh et al. 2010). Additionally, many LEO missions (such as the COSMIC/FORMOSAT-3) also carry dual-frequency GNSS receivers gathering data from a zenithal antenna, in principle intended for precise orbit determination (POD) of the corresponding satellite. These data are direct observations that provide new insights into the topside electron content distribution (Yue et al. 2010b; Liu et al. 2008).

4.3.1 Classical inverse Abel transform

In an occultation scenario (Fig. 7), two assumptions are typically made that simplify the algorithm for refractivity profile retrieval: (1) the spherical symmetry of the free electron density distribution, and (2) neglecting the LEO topside electron

event. The slant total electron content (S) can be expressed in terms of the electron densities (N_e) for each sounded layer and the corresponding lengths (l) (see the text for details)

content contribution. Thus Eq. 30, taking into account Eqs. 31 and 32, becomes:

$$S = \int_{r_T}^{r_R} \frac{r \cdot N_e(r)}{\sqrt{r^2 - p^2}} dr \tag{40}$$

Due to the spherical symmetry assumption, the consecutive rays in an occultation event (see Fig. 7) can be rotated around the geocenter to be represented as parallel lines, sorted by decreasing order of the nearest distance of the given ray to the geocenter (e.g., by impact parameter p ; see Fig. 7).

Due to the second assumption of neglecting the topside electron content, the ionospheric combination of carrier phases L_I (see Eq. 17) can be calibrated from the first observation with a negative elevation in terms of the STEC. The corresponding ambiguity is applied to every ray within the n rays in the occultation (it is further assumed that there are no undetected carrier phase cycle slips; see Hernández-Pajares et al. 2000a for further details). From this set of calibrated STEC values, the electron densities can be derived for each layer defined by the corresponding impact parameter (see Fig. 7), starting from the outer layer, which is defined by the ray number 1:

$$(N_e)_1 = \frac{S_1}{l_{1,1}} \tag{41}$$

with the corresponding crossing length $l_{1,1}$. Thereafter, it is easy to show by recursive solution (see the above-mentioned reference Hernández-Pajares et al. 2000a) that the remaining electron densities can be computed as:

$$(N_e)_j = \frac{1}{l_{j,j}} \left(S_j - \sum_{k=1}^{j-1} (N_e)_k \cdot [l_{j,k} - l_{j,k+1}] \right) \tag{42}$$

where $l_{j,k}$ represents the intersection length between the pierce points of the given ray j with the layer k (again, see Fig. 7).

This discrete formulation is equivalent to the inverse Abel transform that can be expressed in its continuous form as follows:⁵

$$N_e(r) = -\frac{1}{\pi} \int_r^{r_{\text{LEO}}} \frac{dS(p)/dp}{\sqrt{p^2 - r^2}} dp \quad (43)$$

r stands for geocentric distance (associated with the impact parameter of the actual ray) where the electron density is estimated, p is used as the corresponding integration parameter (corresponding to the impact parameters of the rays above the actual ray), and r_{LEO} is the position of the LEO satellite. Note that the electron densities can also be derived from the L_1 Doppler excess phase rate observable (the extra phase change induced by the atmosphere with respect to a straight-line propagation) apart from the ionospheric phase combination, similar to the way neutral refractivity is typically calculated (see, e.g., Aragón-Ángel et al. 2010).

4.3.2 Taking into account the horizontal electron content gradients in the occultation region

Nevertheless, the spherical symmetry assumption (i.e., that the electron density function only depends on height) is a considerable simplification of the problem, particularly because it implies a constant VTEC value over the region where the occultation takes place, a region that can be as large as 3,000 km wide or more. This implication is clearly very unrealistic (see the right panel of Fig. 1).

Various authors have attempted to take into consideration additional information when retrieving the electron density (Yue et al. 2010a; Tsai and Tsai 2004; Hernández-Pajares et al. 2000a). In particular, in the last reference (Hernández-Pajares et al. 2000a), the VTEC is used to describe the horizontal variation of the electron density in the occultation region. The VTEC can be externally obtained from global maps, such as those computed by different agencies for the IGS (see, e.g., Hernández-Pajares et al. 2009a), in IONEX format (Schaer et al. 1998) or from climatological models such as the IRI (Bilitza 2001). In this way, a very significant error reduction of up to 40% can be achieved with the *Improved Abel transform inversion* (García-Fernández et al. 2003b) while maintaining the simplicity of the algorithm, which also includes the estimation of the plasmaspheric contribution (topside), using a dedicated topside model with positive elevation data, a convenience in any Abel inversion approach. This point becomes especially important for low-height (below 450 km) LEO missions such as CHAMP (e.g., Jakowski et al. 2002, 2003).

⁵ See for instance http://en.wikipedia.org/wiki/Abel_Transform.

4.4 Example of a technique for the direct determination of day-to-day STEC variation

To detect ionospheric irregularities, a direct and accurate way of detrending the STEC from GNSS data, with the corresponding value of the previous day, can be used. This technique exploits the repeatability of the GPS transmitter–receiver geometry for permanent ground-based stations in an Earth-fixed reference frame (such as the WGS84 for GPS) after one sidereal day of approximately 23 h and 56 min (i.e., after two orbits of the GPS satellite and one rotation of the Earth). Due to this periodicity, the ionospheric carrier phase ambiguity determination by code leveling is more precise, because most of the typical multipath error is cancelled out. This error is LOS dependent and cancels out by differencing the corresponding measurements (a similar approach, but for precise positioning, can be found in Choi et al. 2004). We summarize the corresponding algorithm, hereinafter the *Day to Day STEC variation* (D2DS) technique (Hernández-Pajares et al. 1997a), based on the dependency of the ionospheric phase and code combinations (see Eqs. 17, 18).

Here, we redefine (with respect to the previous usage in Eq. 30) the operator δ which now represents the consecutive difference before and after two GPS orbits and one Earth rotation:

$$\delta(\circ) \equiv (\circ)_t - (\circ)_{t-23^h56^m} \quad (44)$$

Applying δ to Eqs. 17 and 18 yields:

$$\delta L_I = \alpha \cdot \delta S + \delta B_I \quad (45)$$

$$\delta P_I = \alpha \cdot \delta S + \delta \epsilon_T \quad (46)$$

where it is not necessary to correct the wind-up term that is canceled out (except for a constant part, included in the ambiguity term). More important from the quantitative point of view is the following: on one hand, the interfrequency differential code biases should be almost the same, after 23 h and 56 min and at a similar local time (and, in general, a similar temperature) and, on the other hand, the code multipath error should cancel out.⁶ The only remaining main measurement error term is the thermal one, which has the basic properties of white noise, reducing its effect by a factor \sqrt{n} after averaging over a continuous combined arc of n samples between the previous and the actual sidereal days. This provides a precise, straightforward estimation of the corresponding bias term from Eqs. 45 and 46:

$$\delta \hat{B}_I = \langle \delta L_I - \delta P_I \rangle \quad (47)$$

⁶ The geometry is practically the same after one sidereal day for permanent ground receivers, so the consecutive multipath difference almost cancels out, with the exception of some unusual cases such as sudden changes in the environment of the receiver (e.g., removed trees, a new object close to the antenna, snow or rainstorms).

in such a way that the D2DS variation term $\delta\hat{S}$ can be directly obtained as:

$$\delta\hat{S} = \frac{1}{\alpha}(\delta L_I - \langle \delta L_I - \delta P_I \rangle) \quad (48)$$

and an approximation of the corresponding variation of the VTEC can be obtained from a simple thin layer approximation:

$$\delta\hat{V} \simeq \frac{1}{M}\delta\hat{S} \quad (49)$$

where M is the mapping function for an observation, taken at elevation E at the receiver position with a geocentric distance r and the associated ionospheric pierce point at the geocentric distance r' (see Eq. 32; Fig. 5).

This simple D2DS approach provides an accurate estimation of the STEC variation at the error level of a few TECU and gives the corresponding VTEC variation. This approach has been used by various authors for detecting solar flares (e.g., Liu et al. 2004), and it can contribute to generating reference ionospheric datasets for model evaluation (similar to that reported in Feltens et al. 2010 with STEC variations along the same arc of the phase data).

5 Short-term ionospheric variability based on GNSS observations

As detailed above, the GPS signal is very sensitive to the distribution of free electrons, which responds to the EM field, oscillating and generating a secondary EM wave that interferes and changes the velocity of the GPS signals (the main ionospheric effect on GPS code and phase observations). Due to this fact, GPS is an excellent ionospheric sounding system that has revealed new and detailed views of the electron content distribution, especially in terms of electron content variability, with a duration from many hours (ionospheric storms) to tens of seconds (solar flares) or less (scintillation). Some of these views are briefly summarized in the following.

5.1 Traveling ionospheric disturbances

Traveling ionospheric disturbances (TIDs) are plasma density fluctuations that propagate as waves through the ionosphere at a wide range of velocities and frequencies. TIDs have been observed in most ionospheric measurements: GPS, very large base interferometry (VLBI), incoherent scatter radar (ISR) and Faraday rotation measurements of polarized EM waves transmitted from satellites (which are proportional to electron content and geomagnetic field projection to the LOS). Many authors distinguish between large-scale TIDs (LSTIDs) and medium-scale TIDs (MSTIDs). LSTIDs present a period longer than 1 h and move faster than 300 m/s. They seem to be related to geomagnetic activity and

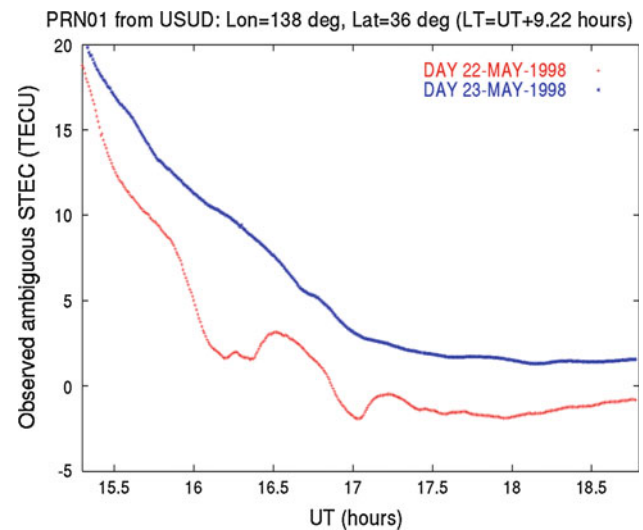


Fig. 8 Large scale traveling ionospheric disturbance (LSTID) directly observed in the ambiguous STEC obtained from the $L_I = L_1 - L_2$ GPS measurement corresponding to satellite PRN01 observed from Usuda, Japan, on the 23rd of May, 1998 (red line). For reference, the corresponding observations are given for the next day (blue line)

Joule-effect heating at high latitudes, which produce thermospheric waves at lower latitudes (see Fig. 8 and Shiokawa et al. 2002 for more details). MSTIDs have shorter periods (from 10 min to 1 h) and are slower moving (50–300 m/s). The origin of MSTIDs seems to be related to meteorological phenomena such as neutral winds or the solar terminator that produce atmospheric gravity waves manifesting as TIDs at ionospheric heights. This type of TID, which more frequently affects space geodesy users, in terms of the season and local time, will be discussed in more detail in the following section.

5.1.1 Medium-scale TIDs

MSTIDs are wave-like signatures appearing in the STEC, with typical amplitudes of several TECU and wavelengths of 100–300 km. MSTIDs show strong seasonal behavior at mid-latitudes, which seems related to the solar terminator and associated atmospheric gravity waves, in such a way that they mostly occur on winter days, moving toward the equator with a typical horizontal velocity of 100–250 m/s, and on summer nights moving westward with velocities of 50–150 m/s (see Hernández-Pajares et al. 2006a). Such strong seasonal behavior allows simple MSTID modeling for practical applications such as precise GNSS navigation (Hernández-Pajares et al. 2006b).

Despite the small amplitude of the MSTIDs, typically of tenths of a TECU in STEC GPS observations, several authors (Chen et al. 2003; Wanninger 2004; Hernández-Pajares et al. 2006b) have shown that the presence of such ionospheric disturbances can cause significant performance degradation in precise GPS navigation. For this reason, the differential ionospheric delays should be predicted with very high precision,

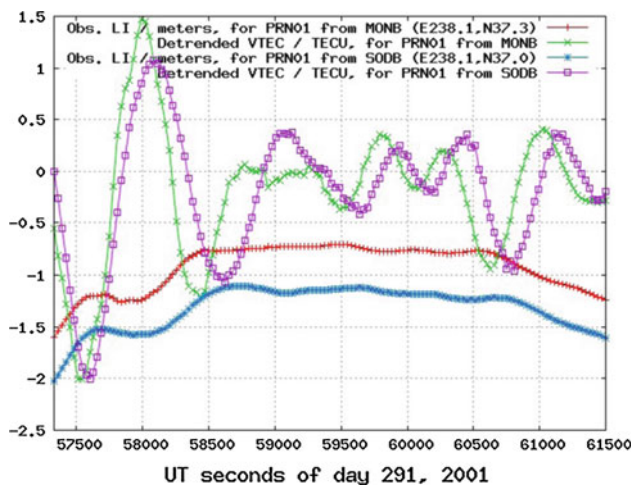


Fig. 9 Two examples of the detrending method acting over two close stations of the Californian network located in the same meridian: MONB, placed at 36 km northern than SODB, detects before the MSTIDs (green and magenta curves, respectively, representing detrended VTEC in TECU). This is in correspondence with the characterization derived in Hernández-Pajares et al. (2006a) for the winter and day time scenario. The original measurements L_I (in m), observed for the same satellite (PRN01) from both receivers MONB and SODB, are also represented in red and blue curves, respectively

at least 0.25 TECU (such as in the case of the wide area real-time kinematic, WARTK,⁷ technique; see, e.g., Hernández-Pajares et al. 2000b, 2010a).

MSTID can very easily be detected at mid-latitudes by simple high-pass filtering or STEC detrending (using, for instance, a consecutive double difference in time every 300 s) of the ionospheric carrier phase L_I (see Fig. 9, which serves as well to illustrate a typical case of MSTID propagation in winter day time).

5.2 Solar flares

Solar flares are one of the most violent events that take place on the sun's surface. They are generated near sunspots and are characterized by the emission of radiation throughout the entire electromagnetic spectrum and by the ejection of charged particles. The radiation produced by a solar flare in the ultraviolet and X-ray bands is especially important for the ionosphere, and it reaches the Earth in approximately 8 min. In contrast, the most part of the ejected particles (a mix-

⁷ WARTK extends the coverage of real-time centimeter error level GNSS positioning from distances of up to tens of kilometers from a master station (provided by the RTK technique) to distances of up to hundreds of kilometers. This improvement is achieved by the generation of (1) a precise real-time ionospheric model from permanent receivers separated by several hundreds of kilometers, (2) an efficient interpolation of such slant ionospheric delays to roving users separated by a few hundreds of kilometers, and (3) an efficient combination of this information with the geodetic information to better determine the carrier phase ambiguities in real-time.

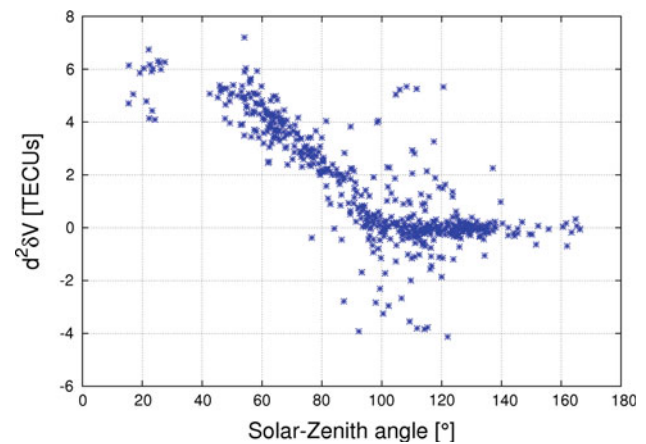


Fig. 10 Dependence of the double consecutive difference of the day-to-day VTEC variation ($d^2\delta V$) on the solar-zenith angle (SZA, at the ionospheric pierce points) for the Halloween storm solar flare precursor (at 11 h and 3 min GPS time). Note that a few number of measurements with SZA between 80° and 120° are affected by scintillations and their $d^2\delta V$ is not close to zero

ture of electrons, protons and heavier nuclei moving with non-relativistic velocities) take 1–2 days to arrive, following the interplanetary magnetic field (IMF) lines. Therefore it is important to emphasize that the radiation reaches the Earth before any particle enhancement occurs, and this delay allows solar flares to serve as predictors of potential ionospheric storms. Moreover, the high energy associated with the radiation produces a sudden increase of ionization in our atmosphere and, by extension, an abrupt increase in the TEC (Mendillo et al. 1974). As the ionization is mainly produced in the ionosphere, one way to detect solar flares is by monitoring the ionospheric TEC using a worldwide network of GNSS receivers (the TEC variation occurs over a large area, in the daylight hemisphere). More details can be found in a recent review (Tsurutani et al. 2009).

The solar flare effect, when a global network is considered, is mostly dependent on the solar-zenith angle (see Fig. 10). One simple and efficient way of detecting solar flares is by applying the day-to-day STEC variation technique (D2DS, see previous section) to detrend the STEC and easily obtain the corresponding VTEC variation from the direct ionospheric carrier phase observations. Double differences in time can allow better detection of the event characteristic times (see the example in Fig. 11 where the simultaneous increase of VTEC is shown for receivers separated thousands of km in daylight hemisphere; details can be found in García-Rigo et al. 2007). Other examples of different approaches are given in Afraimovich et al. 2002 and García-Rigo et al. 2008.

5.3 Ionospheric storms

Large ionospheric storms are among the main disturbances occurring in the ionosphere, and these events are typically

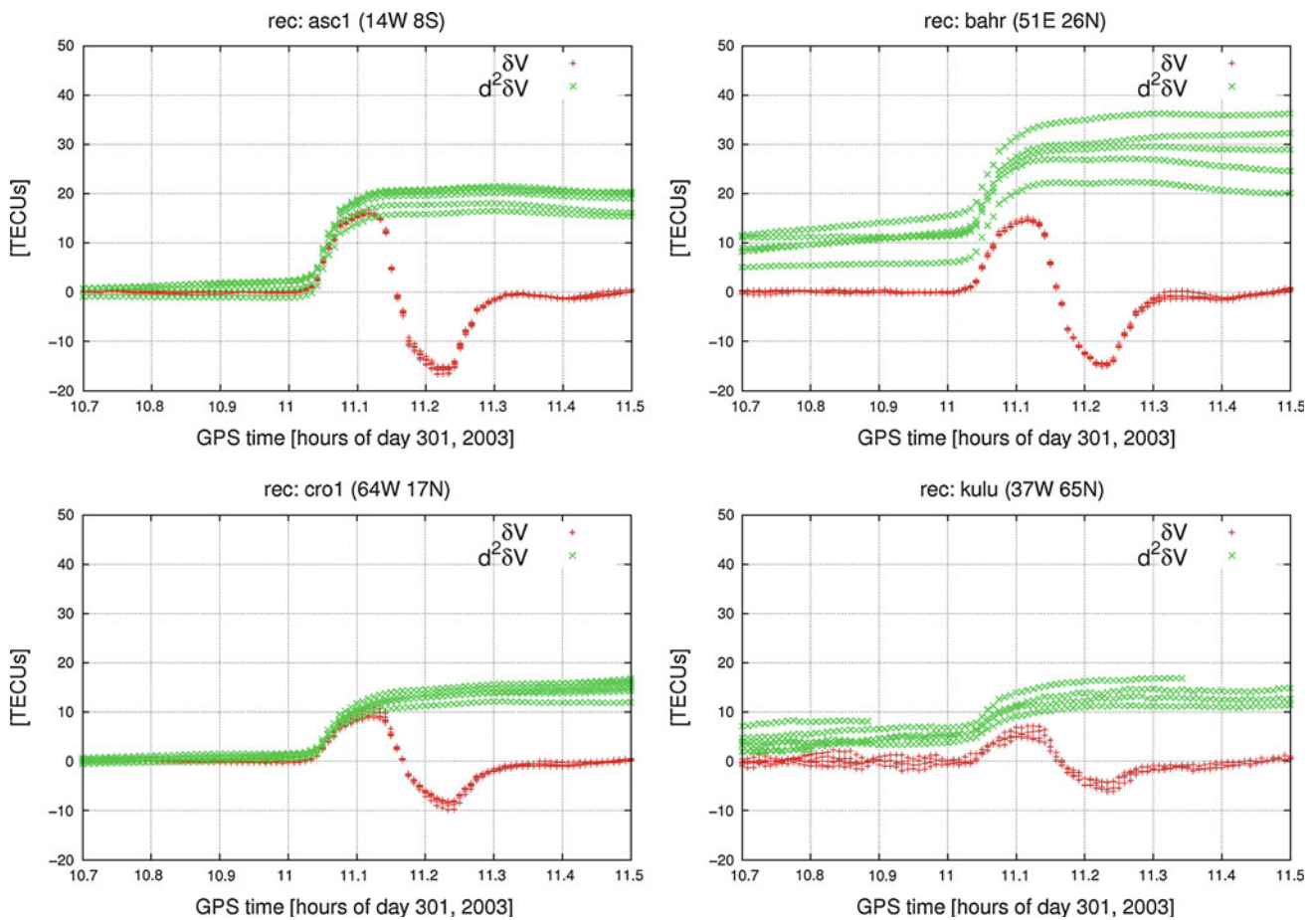


Fig. 11 Day-to-day VTEC variation (δV) and its double consecutive difference in time ($d^2\delta V$), at 30 s observation period and using a slide window of 12 samples, as function of time obtained from the GPS signals gathered by the IGS receivers asc1 (*upper left panel*), bahr (*upper right panel*), cro1 (*lower left panel*) and kulu (*lower right panel*) during

the X-class flare on 28th October, 2003, including all satellites in view above a masking elevation angle of 30° . The longitude, latitude and mean solar zenith angle of each station are respectively $14W, 8S, 23^\circ$, $51E, 26N, 56^\circ$, $64W, 17N, 78^\circ$ and $37W, 65N, 85^\circ$

associated with the arrival of an enhancement of the solar wind, usually with coronal mass ejection (CME) events happening during solar flares, which can produce high temporal and spatial variability of the electron density distribution. This variability occurs particularly when the interplanetary magnetic field component has a southward ecliptic component close to the Earth. In this way, it reconnects with the geomagnetic field, inducing particle precipitation at high latitudes over the auroral regions, producing significant changes in electric fields (for more details, see for example Kelley 2009). One of the most important ionospheric storms ever recorded was the so-called Halloween storm, which occurred on 30th October 2003 (see Coster et al. 2007). Apart from its more dramatic effect in the American sector, with enhancements at the level of many tens of TECUs, an important nighttime enhancement was also reported in the European sector, producing problems in the EGNOS test bed (ESTB) ionospheric modeling and corresponding integrity problems in the satellite based augmentation systems (SBAS)

based positioning; see Fig. 12 and Hernández-Pajares et al. 2005b.

5.4 Scintillation

Ionospheric scintillation can be described as the phenomenon of rapid variation of the refractive index when the trans-ionospheric radio signals cross patches of free ionospheric electrons, producing fading and rapid changes in the carrier phase, such as those of the GNSS. This scintillation can even produce a loss of lock. Scintillation more commonly occurs at low latitudes (see, for example, Basu et al. 1999) at the maximum of the solar cycle, between the local sunset and midnight, and at any time at high latitudes. It is considered one of the main problems that has persisted after GNSS modernization, for public-safety applications, such as the SBAS in civil aviation (see Walter et al. 2010 and the references cited within for more details).

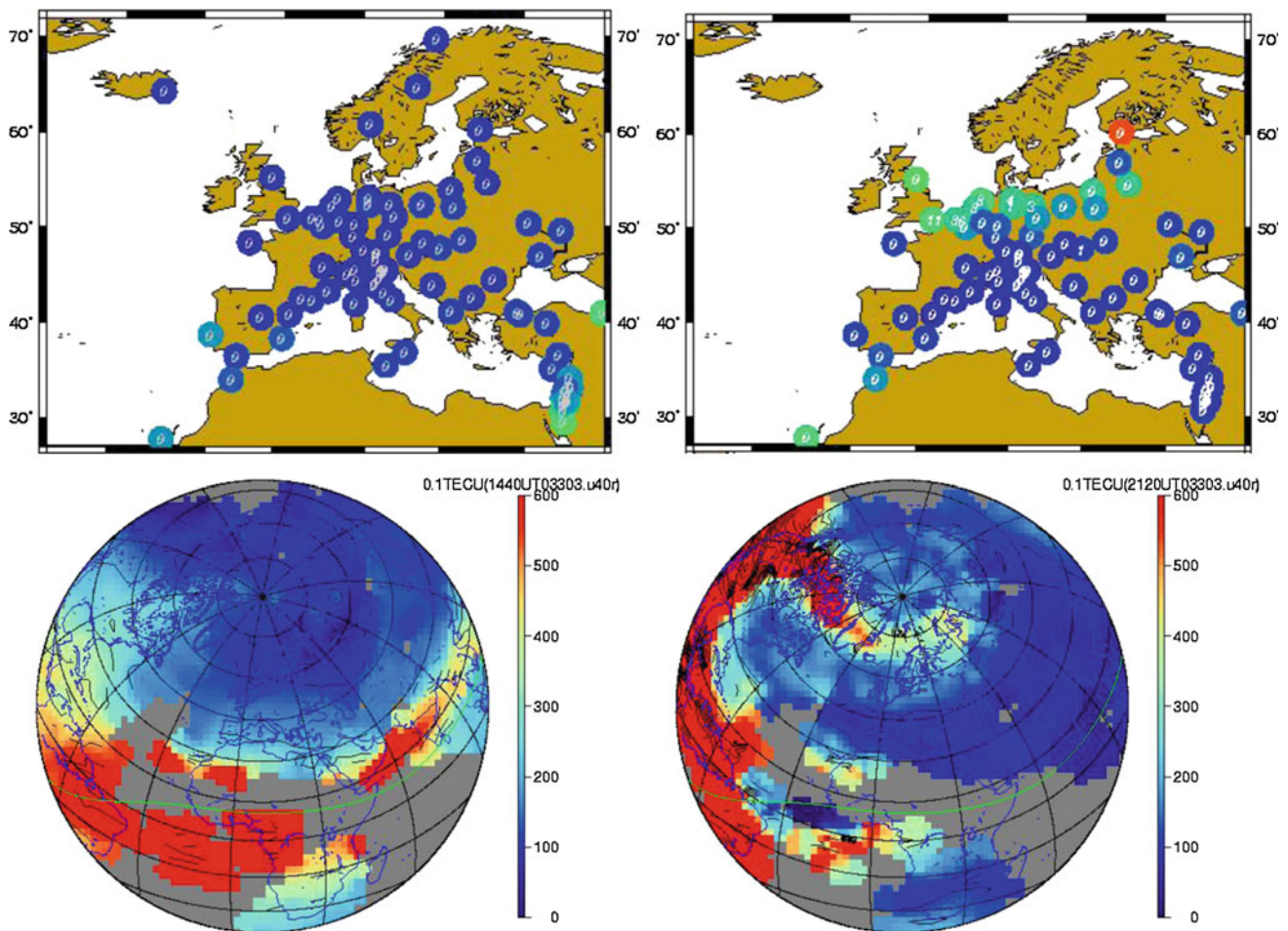


Fig. 12 Increase in the night time electron content in the European sector, as a secondary effect of the Halloween storm on 30th October, 2003 (compare the VTEC map for 2130UT in the *bottom-right plot* with the VTEC map for 1430UT in the *bottom-left plot*). In the *top*

plots, the corresponding events of loss of positioning integrity can be seen in terms of dots for many IGS stations treated as ESTB SBAS users (*non-blue dots* denote the occurrence of missed integrity events)

One way of measuring complete scintillation characteristics is to use GNSS measurements of signal amplitude (power) and phase at a very high sampling rate (such as 50 Hz) to better characterize the given variations, which are typically centered at frequencies above 1 Hz. From these measurements, two indices are generated: the normalized RMS of power (S_4) and the standard deviation of the phase, σ_ϕ (see, e.g., Van Dierendonck and Arbesser-Rastburg 2004).

Several authors suggest that when no high-frequency measurements are available, an alternative way of detecting ionospheric phase scintillation is the rate of total electron content (ROT) and the ROT Index (ROTI), which is defined as the standard deviation of ROT computed from 30-sec data over a time span of 5 min. The ROTI appears to correlate to a certain extent with σ_ϕ (see, e.g., Li et al. 2007 and Beniguel et al. 2009).

An example of scintillation at low latitudes is illustrated in Fig. 13 for the LOS of the several GPS satellites within view of the NTUS IGS receiver [104E,001N], during day 266 of

2004. The STEC values are represented in red, its rate (ROT) in green (computed from the 30-s data) and the ROT index (ROTI) in blue. On this day (22nd September 2004), there was a remarkable scintillation activity from 1400 to 1600 UT, i.e., approximately 2030 to 2230 LT (see the ROTI alone in Fig. 14).

This particular result is compatible with the low-latitude scintillation behavior obtained after computing the ROTI for the last whole solar cycle since 1998 (Fig. 15). It is evident that maximum scintillation activity typically occurs in the local time interval from 2000 to 2300 LT at this equatorial location, especially during the solar cycle maximum.

6 Benefits of ionospheric knowledge for space geodesy

In the previous sections, we attempted to summarize the growing knowledge regarding the distribution of free electron content in the ionosphere. This increase in knowledge

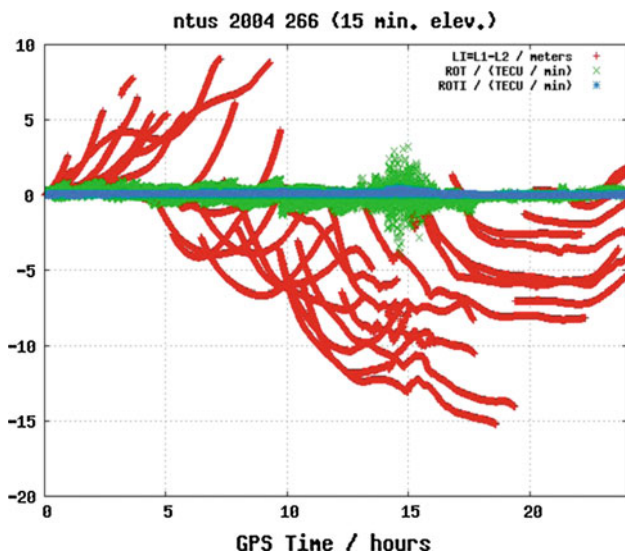


Fig. 13 Different ionospheric parameters sensitive to scintillation activity are presented for the NTUS IGS receiver (104E,001N), on day 266 of 2004; STEC values for the LOS of the different GPS satellites in view are shown in red, its rate (ROT) in green (computed from the 30-s data) and the ROTI in blue (the standard deviation of ROT, computed from 30 s data over a time span of 5 min)

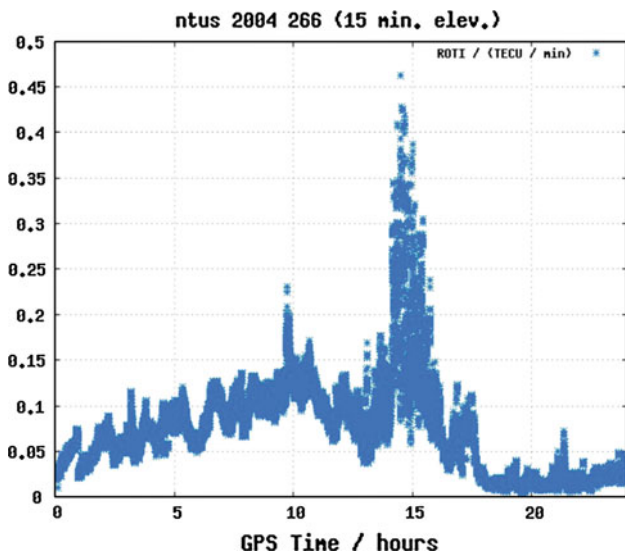


Fig. 14 Enlargement of the previous figure, corresponding to the ROTI alone

has been made possible due to the use of the new space geodetic multifrequency technique, GNSS, with its unprecedented high temporal and spatial sampling rates. An accurate knowledge of ionospheric conditions can in turn be used to improve space geodetic techniques. An example with significant research activity in the last years is the evaluation and application of higher-order ionospheric corrections, which are briefly introduced below. Other benefits more focused on improving GNSS are also summarized. We consider that GNSS, the technique that has contributed the most to advancing our understanding of the ionosphere in the

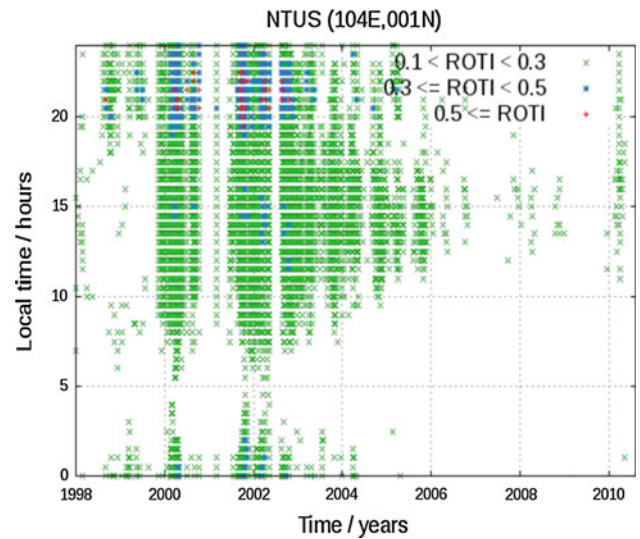


Fig. 15 Occurrence of high values of the ROTI, in terms of time (*horizontal axis* in years) and local time (*vertical axis*, in h) for NTUS receiver

last decades, is at the same time the technique that has most benefited from improved knowledge of the electron content distribution in time and space.

6.1 Higher-order ionospheric corrections

One general application of a good knowledge of the ionospheric free electron content distribution is the correction of higher-order ionospheric effects for high-precision space geodesy. For example, L_c (see Eq. 21) is the main observable used in precise GPS positioning. But this combination of carrier phase measurements only corrects the first-order ionospheric term as it has been indicated above, and the high order ionospheric terms can be greater than 1 cm in such combination. If the goal is to achieve a precision at millimeter level, the higher order ionospheric terms (especially the second order term) must be taken into account consistently in the positioning model and products used (such as satellite clocks and orbits).

Indeed, following Eqs. 7–10 and 12, a good knowledge of STEC combined with a reasonable magnetic field model (such as IGRF; see, for example, Tsyganenko 2003) allows us to approximate the second- and third-order ionospheric terms so that they can be removed from the carrier (and code) measurements. In this regard, two main possible strategies can be considered:

1. Taking STEC from VTEC maps computed from actual data, e.g., from IGS analysis centers, as described in Kedar et al. 2003 and in Fritsche et al. 2005 (this approach is applicable to any space geodetic technique).
2. In the case of corrections to GNSS dual frequency measurements, taking STEC from the same dual frequency

ionospheric measurement (i.e., ionospheric phase combination, aligned with the corresponding combination of dual-frequency codes). Only a knowledge of the DCBs for both the receiver and the transmitter (both values are very stable in time) is needed. In this way, despite that alignment errors due to multipath and thermal noise in the code can have an effect, we avoid the lack of accuracy of an ionospheric mapping function, especially at low latitudes and/or in low-elevation scenarios (when the higher-order ionospheric effects are more important); see [Hernández-Pajares et al. 2007](#). By correcting the higher-order ionospheric terms, the corresponding *contamination* (biasing) of geodetic products is prevented. This case is particularly true for the GNSS satellite products (such as orbits and clocks), with their associated errors of up to few centimeters (see, for example, [Hernández-Pajares et al. 2007](#)).

6.2 High-precision GNSS real-time positioning

An example of how the precise knowledge of the STEC provides a significant advantage for real-time GNSS users seeking precise (decimeter error level) navigation can be found in WARTK. Indeed, the main challenge is the rapid carrier phase ambiguity fixing in real-time conditions, enabling navigation with the first-order ionospheric-free combination of carrier phases (L_c , see Eq. 21), the main observable capable of supporting this ambitious requirement. In addition to L_c which is the main data required for precise navigation, additional information is needed to quickly fix the corresponding phase ambiguities. Indeed, to be able to apply Eq. 28 and so yield a rapid and sufficiently accurate estimation of the L_c ambiguity, B_c , the user needs (among the DCBs estimates, which are quite stable over a period of hours): (1) the Melbourne-Wübbena combination providing a proxy for the widelane phase ambiguity (Eqs. 20, 26); and (2) the slant TEC, provided externally by a dedicated central processing facility (CPF). This CPF can typically provide the STEC, fulfilling the high-precision requirements for rapid phase ambiguity fixing (i.e., to better than 0.25 TECU). This procedure has been demonstrated in the WARTK technique by combining a tomographic and MSTID technique in the GNSS' data processing from a wide-area network. Such a network is composed of permanent multifrequency GNSS receivers separated by up to many hundreds of kilometers (see for more details, [Hernández-Pajares et al. 2000b, 2002, 2003, 2006b, 2010a](#)).

6.3 Single antenna GNSS orientation

A new specialized application of a good real-time knowledge of the density of the number of free electrons in the ionosphere is the estimation of the GNSS user orientation

(or attitude) with a single antenna and receiver (instead of from the usual minimum of two nearby antennas) by applying Eq. 17: indeed, as demonstrated by [Hernández-Pajares et al. \(2004\)](#), in this way, the wind-up ϕ (carrier phase polarization rotation) can be accurately measured in real time, with most random errors remaining as small as a few degrees. Thus, an additional product (e.g., for WARTK users) can be obtained, which can also be efficiently combined with inexpensive micro-electromechanical systems (MEMS) inertial sensors, which are typically affected by significant drift errors.

6.4 Real-time GNSS meteorology

Another potential advantage of our improved knowledge of the ionospheric STEC for the GNSS LOS in permanent multifrequency receivers, and of the corresponding strong reduction of convergence time in the computation of B_c , is its capability to provide accurate estimates of zenith tropospheric delay. These estimates can be made in real time from a warm start, or after a few minutes from a cold start representing a significant improvement, compared with the time typically needed for B_c convergence in permanent receivers (i.e., up to 1 h). This method can be applied for receivers separated by up to many hundreds of kilometers (see [Hernández-Pajares et al. 2001](#)). This dramatic reduction could be used to incorporate very fresh data (in this case, zenith tropospheric delay values) into weather forecasting models, with a corresponding increase in their effectiveness.

6.5 Recent results

The study and estimation of the ionosphere from the GNSS perspective and the application to space geodesy are growing and active fields. In this context, it is worth noting several reports of very recent representative works that have occurred during the publication process of this paper. From the viewpoint of ionospheric studies, we can cite, for instance, a recent paper providing a potential physical explanation for the semi-annual anomaly ([Azpilicueta and Brunini 2011](#)). Regarding the application of our understanding of the ionospheric state to space geodesy, we can highlight two remarkable recent examples, one discussing in detail different higher-order ionospheric effects in GPS ([Petrie et al. 2011](#)), and another highlighting the application of these effects to problems such as long time series of accurate GPS coordinates in general, and in the provision of accurate models of glacial isostatic adjustment (GIA) in particular ([King et al. 2010](#)).

From an operational standpoint, it is worth emphasizing the development of a new generation of IGS ionospheric prediction maps: among those already computed by CODE, ESA and UPC have recently started its computation (see, e.g., [García-Rigo et al. 2009](#)). In addition, the forthcoming real-time ionospheric VTEC maps, presently computed internally

by JPL, are currently in the process of being implemented as a potential future IGS product, within the context of RT-IGS pilot project products (Caissy et al. 2011). Finally, in parallel, studies and initiatives on combining different types of ionospheric data are also moving forward, e.g., the combination of ground- and LEO-based GNSS data and dual-frequency satellite altimetric measurements (Alizadeh et al. 2010).

7 Conclusions

This paper summarizes some of the main ionospheric modeling aspects and their effects on space geodetic techniques. This work was based on GNSS, which due to their unique spatial and temporal sounding capabilities, have become a key technology leading to significant advances in ionospheric sounding. Simultaneously, we have attempted to show how GNSS is being improved due to our better understanding of ionospheric conditions.

Acknowledgments This work was partially supported by the IBERWARTK (ESP2007-62676) and Antartica (CTM2010-21312-C03-02) projects funded by the Spanish Ministry of Science and Innovation, and was done coinciding with the AGIM and MONITOR activities, organized and funded by the ESOC- and ESTEC-ESA centers, respectively. The authors are thankful to the associate editor and reviewers for all the detailed suggestions which have been very important to improve the manuscript. The authors appreciate as well the suggestions kindly given by Dr. Metin Nohutcu to the final version.

References

- Afraimovich EL, Altynsev AT, Grechnev VV, Leonovich LA (2002) The response of the ionosphere to faint and bright solar flares as deduced from global GPS network data. *Ann Geophys* 45(1):31–40
- Alizadeh M, Schuh H, Schmidt M (2010) Multi-dimensional modeling of electron density using spherical harmonics and chapman function, held in Vienna. In: *Geophysical Research Abstracts*, vol 12, EGU2010-4103-1, EGU General Assembly, May 2010
- Angling MJ, Cannon PS (2004) Assimilation of radio occultation measurements into background ionospheric models. *Radio Sci* Vol 39. RS1S08, doi:10.1029/2002RS002819
- Aragón-Ángel A, Hernández-Pajares M, Juan JM, Sanz J (2010) Improving the Abel transform inversion using bending angles from FORMOSAT-3 /COSMIC. *GPS Solut* 14:23–33. doi:10.1007/s10291-009-0147-y
- Arikan F, Arikan O, Erol CB (2007) Regularized estimation of TEC from GPS data for certain midlatitude stations and comparison with the IRI model. *Adv Space Res* 39(5):867–874
- Azpilicueta F, Brunini C, Radicella SM (2006) Global ionospheric maps from GPS observations using modip latitude. *Adv Space Res* 38:2324–2331
- Azpilicueta F, Brunini C (2011) A new concept regarding the cause of ionosphere semiannual and annual anomalies. *J Geophys Res Space Phys* 116:A01307. doi:10.1029/2010JA015977
- Basu S, Groves KM, Quinn JM, Doherty P (1999) A comparison of TEC fluctuations and scintillations at Ascension Island. *J Atm Solar Terr Phys* 61:1219–1226
- Beniguel Y, Adam J-P, Jakowski N, Noack T, Wilken V, Valette J-J, Cueto M, Bourdillon A, Lassudrie-Duchesne P, Arbesser-Rastburg B (2009) Analysis of scintillation recorded during the PRIS measurement campaign. *Radio Sci* 44:RS0A30. doi:10.1029/2008RS004090
- Bilitza D (2001) International reference ionosphere 2000. *Radio Sci* 36(2):261–275
- Brunini C, Van Zele MA, Meza A, Gende M (2003) Quiet and perturbed ionospheric representation according to the electron content from GPS signals. *J Geophys Res* 108(A2):1056. doi:10.1029/2002JA009346
- Bust GS, Mitchell CN (2008) History, current state, and future directions of ionospheric imaging. *Rev Geophys* 46: 2006RG000212, RG1003
- Caissy M, Weber G, Agrotis L, Wübbena G, Hernández-Pajares M (2011) The IGS real-time pilot project—the development of real-time IGS correction products for precise point positioning. In: *Geophysics Research Abstracts*, vol 13, EGU2011-7472, EGU General Assembly, May 2011
- Chen X, Landau H, Vollath U (2003) New tools for network RTK intergrity monitoring. In: Paper presented at ION GPS/2003. Inst. of Navig., Portland, Oregon, USA
- Choi K, Bilich K, Larson M, Axelrad P (2004) Modified sidereal filtering: implications for high-rate GPS positioning. *Geophys Res Lett* 31:L22608. doi:10.1029/2004GL021621
- Ciraolo L, Azpilicueta F, Brunini C, Meza A, Radicella S (2007) Calibration error son experimental slant total electron content (TEC) determined with GPS. *J Geod* 81:111–120
- Coster AJ, Colerico MJ, Foster JC, Rideout W, Rich F (2007) Longitude sector comparisons of storm enhanced density. *Geophys Res Lett* 34:L18105
- Davies K (1990) *Ionospheric radio*. Peter Peregrinus Ltd, London. ISBN 0-86341-186-X
- Dow J, Neilan R, Rizos C (2009) The international GNSS service in a changing landscape of global navigation satellite systems. *J Geod* 83(3–4):191–198. doi:10.1007/s00190-008-0300-3
- Du Q, Faber V, Gunzburger M (1999) Centroidal Voronoi tessellations: applications and algorithms. *SIAM Rev* 41(4):637–676
- Durmaz M, Onur Karslioglu M, Nohutcu M (2010) Regional VTEC modeling with multivariate adaptive regression splines. *Adv Space Res* 46(2):180–189
- Feltens J (2007) Development of a new three-dimensional mathematical ionosphere model at European Space Agency/European Space Operations Centre. *Space Weather* 5:S12002
- Feltens J, Angling M, Jakowski N, Mernandez-Pajares M, Zandbergen R (2010) GNSS contribution to next generation global ionospheric monitoring. *Beacon Satellite Symposium 2010*, Barcelona, 8 June 2010
- Fritsche M, Dietrich R, Knöfel C, Rülke A, Vey S, Rothacher M, Steigenberger P (2005) Impact of higher-order ionospheric terms on GPS estimates. *Geophys Res Lett* 32:L23311
- García-Fernández M, Hernández-Pajares M, Juan JM, Sanz J, Orús R, Coisson P, Nava B, Radicella SM (2003a) Combining ionosonde with ground GPS data for electron density estimation. *J Atm Sol Terr Phys* 65:683–691
- García-Fernández M, Hernández-Pajares M, Juan JM, Sanz J (2003b) Improvement of ionospheric electron density estimation with GPSMET occultations using Abel inversion and VTEC information. *J Geophys Res Space Phys* 108(A9):1338. doi:10.1029/2003JA009952
- García-Rigo A, Hernández-Pajares M, Juan JM et al (2007) Solar flare detection system based on global positioning system data: first results. *Adv Space Res* IRI05-35 39:889–895
- García-Rigo A, Hernández-Pajares M, Juan JM, Sanz J (2008) Real time ionospheric TEC monitoring method applied to detect solar

- flares (Poster). European General Assembly (EGU), Vienna, Austria
- García-Rigo A, Hernández-Pajares M, Monte E, Juan JM, Sanz J, Krankowski A, Wielgosz P (2009) Assessment of UPC model for ionosphere VTEC prediction (Poster). Geodesy for Planet Earth (IAG), Buenos Aires, Argentina
- Ge M, Gendt G, Rothacher M, Shi C, Liu J (2008) Resolution of GPS carrier-phase ambiguities in precise point positioning (PPP) with daily observations. *J Geod* 82(7):389–399. doi:[10.1007/s00190-007-0187-4](https://doi.org/10.1007/s00190-007-0187-4)
- Hajj GA, Ibanez-Meir R, Kursiniski ER, Romans LJ (1994) Imaging the ionosphere with the global positioning system. *Int J Imag Syst Technol* 5:174–184
- Hajj GA, Wilson BD, Wang C, Pi X, Rosen LG (2004) Data assimilation of ground GPS total electron content into a physics-based ionospheric model by use of the Kalman filter. *Radio Sci* 39:RS1S05
- Hernández-Pajares M (2004) IGS ionosphere WG Status report: performance of IGS ionosphere TEC maps, Position Paper. IGS Workshop, Bern
- Hernández-Pajares M, Juan JM, Sanz J (1997) High resolution TEC monitoring method using permanent ground GPS receivers. *Geophys Res Lett* 24(13):1643–1646
- Hernández-Pajares M, Juan JM, Sanz J (1997) Neural network modeling of the ionospheric electron content at global scale using GPS data. *Radio Sci* 32(3):1081–1089
- Hernández-Pajares M, Juan JM, Sanz J, Solé JG (1998) Global observation of the ionospheric electronic response to solar events using ground and LEO GPS data. *J Geophys Res* 103(A9):20789–20796
- Hernández-Pajares M, Juan JM, Sanz J (1999) New approaches in global ionospheric determination using ground GPS data. *J Atm Sol Terr Phys* 61:1237–1247
- Hernández-Pajares M, Juan JM, Sanz J (2000) Improving the Abel inversion by adding ground GPS data to LEO radio occultations in ionospheric sounding. *Geophys Res Lett* 27(16):2473–2476
- Hernández-Pajares M, Juan JM, Sanz J, Colombo OL (2000) Application of ionospheric tomography to real-time GPS carrier-phase ambiguities resolution at scales of 400–1000 km and with high geomagnetic activity. *Geophys Res Lett* 27(13):2009–2012
- Hernández-Pajares M, Juan JM, Sanz J, Colombo OL, van der Marel H (2001) A new strategy for real-time integrated water vapor determination in WADGPS networks. *Geophys Res Lett* 28(17):3267–3270
- Hernández-Pajares M, Juan JM, Sanz J, Colombo OL (2002) Improving the real-time ionospheric determination from GPS sites at very long distances over the equator. *J Geophys Res* 107:A10
- Hernández-Pajares M, Juan JM, Sanz J, Colombo OL (2003) Feasibility of wide-area subdecimeter navigation with GALILEO and Modernized GPS. *IEEE Trans Geosci Remote Sens* 41(9):2128–2131
- Hernández-Pajares M, Juan JM, Sanz J, García-Rodríguez A, Colombo OL (2004) Wide area real time kinematics with Galileo and GPS signals. ION-GNSS meeting, Portland, Oregon
- Hernández-Pajares M, Juan JM, Sanz J, García-Fernández M (2005a) Towards a more realistic ionospheric mapping function. XXVIII URSI General Assembly, Delhi
- Hernández-Pajares M, Juan JM, Sanz J, Farnworth R, Soley S (2005b) EGNOS test bed ionospheric corrections under the October and November 2003 Storms. *IEEE Trans Geosci Remote Sens* 43(10):2283–2293
- Hernández-Pajares M, Juan JM, Sanz J (2006) Medium-scale traveling ionospheric disturbances affecting GPS measurements: Spatial and temporal analysis. *J Geophys Res* 111:A07S11
- Hernández-Pajares M, Juan JM, Sanz J (2006b) Real time MSTIDs modelling and application to improve the precise GPS and GALILEO navigation. ION GNSS meeting, Forth Worth, TX, USA
- Hernández-Pajares M, Juan JM, Sanz J, Orús R (2007) Second-order ionospheric term in GPS: implementation and impact on geodetic estimates. *J Geophys Res* 112:B08417
- Hernández-Pajares M, Juan JM, Sanz J, Orús R, García-Rigo A, Felten J, Komjathy A, Schaer SC, Krankowski A (2009) The IGS VTEC maps: a reliable source of ionospheric information since 1998. *Special IGS Issue J Geod* 83:263–275
- Hernández-Pajares M, Juan JM, Sanz J, Aragón-Ángel A, Ramos-Bosch P, Samson J, Tossaint M, Albertazzi M, Odijk D, Teunissen PJG, de Bakker P, Verhagen S, van der Marel H (2010a) Wide-Area RTK High Precision Positioning on a Continental Scale. Inside GNSS
- Hernández-Pajares M et al (2010b) Section 9.4 Ionospheric model for radio techniques of Chapter 9 Models for atmospheric propagation delays of IERS Conventions 2010. In: Petit G., Luzum B. (eds) IERS Technical Note No. 36. Verlag des Bundes amts für Kartographie und Geodäsie, Frankfurt am Main
- Hofmann-Wellenhof B, Lichtenegger H, Wasle E (2008) GNSS—Global navigation satellite systems: GPS, GLONASS, Galileo & more. Springer, New York
- Hoque MM, Jakowski N (2008) Mitigation of higher order ionospheric effects on GNSS users in Europe. *GPS Solut* 12(2):87–97
- Howe BM, Runciman K, Secan JA (1998) Tomography of the ionosphere: four-dimensional simulations. *Radio Sci* 33:109–128
- Jakowski N, Porsch F, Mayer G (1994) Ionosphere-induced-Ray-Path bending effects in precision satellite positioning systems. *SPN* 1/94:6–13
- Jakowski N, Wehrenpennig A, Heise S, Reigber CH, Lühr H, Grunwaldt L, Meehan T (2002) GPS radio occultation measurements of the ionosphere from CHAMP: early results. *Geophys Res Lett* 29(10). doi:[10.1029/2001GL014364](https://doi.org/10.1029/2001GL014364)
- Jakowski N, Wehrenpennig A, Heise S, Reigber CH, Lühr H (2003) Status of ionospheric radio occultation CHAMP data analysis and validation of higher level data products, First CHAMP science mission results for gravity. In: Reigber Ch, Lühr H, Schwintzer P (eds) *Magnetic and Atmospheric Studies*. Springer, Berlin, pp 462–472. ISBN 3-540-00206-5
- Juan JM, Rius A, Hernández-Pajares M, Sanz J (1997) A two-layer model of the ionosphere using global positioning system data. *Geophys Res Lett* 24(4):393–396
- Kedar S, Hajj GA, Wilson BD, Hefflin MB (2003) The effect of the second order GPS ionospheric correction on receiver positions. *Geophys Res Lett* 30(16):1829. doi:[10.1029/2003GL017639](https://doi.org/10.1029/2003GL017639)
- Kelley MC (2009) The earth's ionosphere: plasma physics and electrodynamics. *Int Geophys Ser* 96. ISBN 978-0-12-088425-4, Elsevier
- Khattatov B, Murphy M, Gnedin M, Sheffel J, Adams J, Cruickshank B, Yudin V, Fuller-rowell T, Retterer J (2006) Ionospheric nowcasting via assimilation of GPS measurements of ionospheric electron content in a global physics-based time-dependent model. *Q J Royal Meteorol Soc* 131(613):3543–3559
- King MA, Altamimi Z, Boehm J, Bos M, Dach R, Elosegui P, Fund F, Hernández-Pajares M, Lavalée D, Mendes Cerveira PJ, Penna N, Riva REM, Steigenberger P, van Dam T, Vittuari L, Williams S, Willis P (2010) Improved constraints on models of glacial isostatic adjustment: a review of the contribution of ground-based geodetic observations. *Surv Geophys* 31:465–507. doi:[10.1007/s10712-010-9100-4](https://doi.org/10.1007/s10712-010-9100-4)
- Kliore AJ, Levy GS, Cain DL, Fjeldbo G, Rasool I (1967) Atmosphere and ionosphere of Venus from the Mariner VS-band radio occultation Measurement. *Science* 158(3809):1683–1688
- Komjathy A, Langley RB (1996) The effect of shell height on high precision ionospheric modelling using GPS. International GPS Service for Geodynamics (IGS) Workshop in Silver Spring, MD, 19–21 Mar 1996. In: *Proceedings of the 1996 IGS Workshop*, pp 193–203

- Li G, Ning B, Yuan H (2007) Analysis of ionospheric scintillation spectra and TEC in the Chinese low latitude region. *Earth Planets Space* 59:279–285
- Liu L, He M, Wan W, Zhang ML (2008) Topside ionospheric scale heights retrieved from Constellation Observing System for Meteorology, Ionosphere, and Climate radio occultation measurements. *J Geophys Res* 113:A10304. doi:[10.1029/2008JA013490](https://doi.org/10.1029/2008JA013490)
- Liu JY, Lin CH, Tsai HF, Liou YA (2004) Ionospheric solar flare effects monitored by the ground-based GPS receivers: Theory and observation. *J Geophys Res* 109:A01307
- Mannucci A, Wilson B, Yuan D, Ho C, Lindqwister U, Runge T (1998) A global mapping technique for GPS-derived ionospheric total electron content measurements. *Radio Sci* 33(3):565–582. doi:[10.1029/97RS02707](https://doi.org/10.1029/97RS02707)
- Mendillo M, Klobuchar JA, Fritz RB (1974) Behavior of the ionospheric F region during the great solar flare of August 7, 1972. *J Geophys Res* 79:665–672
- Misra P, Enge P (2004) *Global positioning system: signals, measurements and performance*, 2nd edn. Ganga-Jamuna Press Lincoln, USA
- Orús R, Hernández-Pajares M, Juan JM, Sanz J (2005) Improvement of global ionospheric VTEC maps by using kriging interpolation technique. *J Atm Sol Terr Phys* 67(16):1598–1609
- Petrie EJ, Hernández-Pajares M, Spalla P, Moore P, King MA (2011) A review of higher order ionospheric refraction effects on dual frequency GPS. *Surv Geophys* 32:197–253. doi:[10.1007/s10712-010-9105-z](https://doi.org/10.1007/s10712-010-9105-z)
- Sanz J, Juan JM, Hernández-Pajares M (2011) GNSS data processing. In: ESA Communication Production Office (ed) *Fundamentals and Algorithms*, vol I (in press)
- Sardon E, Rius A, Zarraoa N (1994) Estimation of the transmitter and receiver differential biases and the ionospheric total electron content from Global Positioning System observations. *Radio Sci* 29:577–586
- Schaer S, Gurtner W, Feltens J (1998) IONEX: The IONosphere Map EXchange Format Version 1. February 25, 1998. In: *Proceedings of the 1998 IGS Analysis Centers Workshop, ESOC, Darmstadt, Germany, February 9–11*, pp 233–247
- Schaer S (1999) *Mapping and predicting the earth's ionosphere using the global positioning system*. Ph. D. Dissertation, Astronomical Institute, University of Berne, Berne, Switzerland, 25 March 1999
- Schmidt M, Bilitza D, Shum CK, Zeilhofer C (2008) Regional 4-D modeling of the ionospheric electron density. *Adv Space Res* 42(4):782–790
- Seeber G (1993) *Satellite geodesy: foundations, methods, and applications*. Walter de Gruyter & Co., Berlin
- Shiokawa K, Otsuka Y, Ogawa T, Balan N, Igarashi K, Ridley AJ, Knipp DJ, Saito A, Yumoto K (2002) A large-scale traveling ionospheric disturbance during the magnetic storm of 15 September 1999. *J Geophys Res* 107(A6):1088. doi:[10.1029/2001JA000245](https://doi.org/10.1029/2001JA000245)
- Smith DA, Araujo-Pradere EA, Minter C, Fuller-Rowell T (2008) A comprehensive evaluation of the errors inherent in the use of a two-dimensional shell for modeling the ionosphere. *Radio Sci* 43:RS6008
- Tsai LC, Tsai WH (2004) Improvement of GPS/MET ionospheric profiling and validation using the Chung-Li ionosonde measurements and the IRI mode. *TAO* 15(4):589–607
- Tsurutani BT, Verkhoglyadova OP, Mannucci AJ, Lakhina GS, Li G, Zank GP (2009) A brief review of solar flare effects on the ionosphere. *Radio Sci* 44:RS0A17. doi:[10.1029/2008RS004029](https://doi.org/10.1029/2008RS004029)
- Tsyganenko NA (2003) A set of FORTRAN subroutines for computations of the geomagnetic field in the Earth's magnetosphere (Geopack). Univ. Space Res. Assoc., Columbia Md., USA
- Van Dierendonck AJ, Arbesser-Rastburg B (2004) Measuring ionospheric scintillation in the equatorial region over Africa, including measurements from SBAS geostationary satellite signals. In: *Proceedings of ION GNSS 17th technical meeting of the satellite division*, Long Beach, CA, vol 316
- Walter T et al (2010) Effect of ionospheric scintillations on GNSS—a white paper. SBAS Ionospheric Working Group, November 2010
- Wanninger L (2004) Ionospheric disturbance indices for RTK and network RTK positioning. In: *Paper presented at ION GPS/2004, Inst. of Navig., Long Beach, California*
- Ware RH, Exner ML, Herman BM, Kuo B, Meehan TK, Rocken C (1995) *GPS/MET preliminary report*. The University Corporation for Atmospheric Research, Boulder, Colorado
- Yue X, Schreiner WS, Lei J, Sokolovskiy SV, Rocken C, Hunt DC, Kuo YH (2010) Error analysis of Abel retrieved electron density profiles from radio occultation measurements. *Ann Geophys* 28:217–222
- Yue X, Schreiner WS, Lei J, Rocken C, Kuo YH, Wan W (2010) Climatology of ionospheric upper transition height derived from COSMIC satellites during the solar minimum of 2008. *J Atm Sol Terr Phys* 72:1270–1274